Photoacoustic Tomography Using a Novel Planar Detector Based on a Michelson Interferometer

Author:
Rory Speirs

Supervisor:
Dr. Alexis Bishop

A thesis submitted in partial fulfilment of the requirements for the degree of Bachelor of Science (Science Scholar Program) (Honours)
in the School of Physics of
Monash University

November 5, 2010

MONASH University

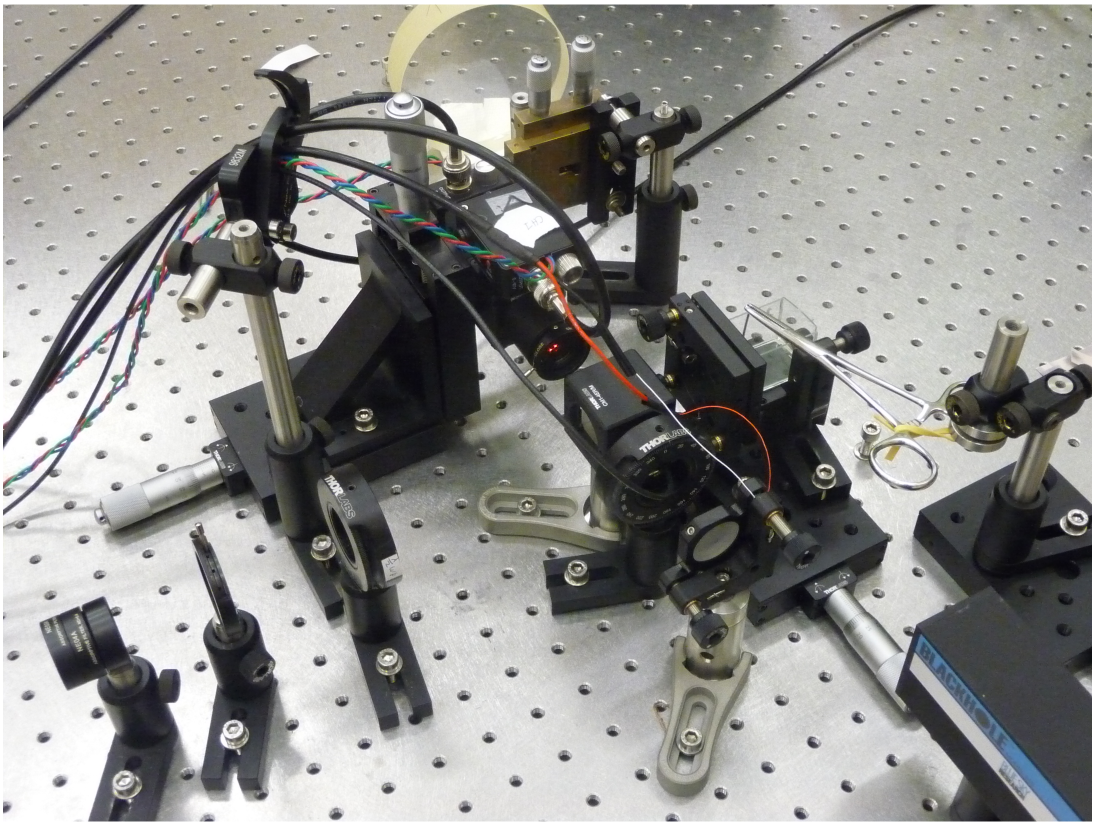

The optical components of the photoacoustic tomography system built in this project.

Abstract

This project involved the development of a novel detector for use in photoacoustic (PA) tomography. The detector was based on a Michelson interferometer, where one of the mirrors acted as the ultrasound sensor. Quadrature phase detection was employed to increase the sensitivity of the system, so the nanometre particle displacements of PA waves could be resolved. The design of the sensing mirror was critical to faithful detection of PA signals. The mirror was made from a thin (150 μm) glass substrate to avoid surface waves and internal reflections. Preliminary measurements made on blood vessel phantoms gave 2D reconstructions with a resolution of less than 1 mm to depths of 6 mm. It was shown that the system should be capable of full 3D tomography, with resolution equal to or greater than other detectors in the literature, and that it should have an advantage in terms of data acquisition speeds. More work is required to evaluate if the detector is sensitive enough be useful in clinical applications.

Contents

Chapter 1

Introduction

High resolution imaging of vascular structure beneath the human skull has the potential to be an important medical diagnostic tool. Existing techniques such as CT, MRI or ultrasound, lack the sub millimetre resolution needed to identify small individual blood vessels which may be of significant consequence regarding diagnosis of early stage cancers or stroke[1].

High resolution imaging of vascular structure has been achieved with the relatively new technique of *optical coherence tomography*, which relies on photons that have been scattered only once during propagation through tissue[2]. The penetration depth of this technique is of the order of hundreds of micrometers in turbid tissue, though it can be increased to $\approx$ 1mm if photons are accepted, which have only a low degree of additional scattering. Imaging of the human brain however is not achievable with this technique due to the high optical scattering efficiency of the skull. Imaging of a mouse brain has been achieved, but only by removing sections of the skull[3].

Photoacoustic (PA) imaging is a hybrid imaging technique, with the potential to give the resolution of optical methods, with the penetration depth of ultrasound. It is an ultrasound imaging technique where the source of the acoustic disturbance is generated by the object being imaged, rather than externally, as is utilised in conventional ultrasound imaging.

Photoacoustic (also referred to as Optoacoustic) techniques produce ultrasound by the *Photoacoustic effect*. This process involves a number of steps: Initially, the object is illuminated by a pulse of electromagnetic radiation which is usually visible or infrared light, though microwaves have also been used[4]. The object absorbs some fraction of this light, which raises its temperature. This increase in temperature subsequently causes rapid thermal expansion of the object, which in turn creates acoustic waves[5]. This is also known as thermoelastic sound generation, since the object is elastically, rather than permanently deformed.

The acoustic waves propagate through biological tissue with only weak attenuation and scattering, with a characteristic length of several centimetres. By detecting the propagated acoustic field, an image of the absorbing object can be produced via tomographic reconstruction.

Though this technique is not strictly limited to biomedical applications[6], most development has been in this direction[7]. This is in part due to a current lack of imaging modality which has both high resolution, and high penetration depth in turbid human tissue.

As yet, no PA system has been produced which is capable of imaging vascular structure within the human brain. However imaging of blood vessels has been achieved *in vivo* on a human hand, and a mouse brain to depths of $\approx$ 1cm. The major difficulty with PA imaging in general is detecting the very small amplitude acoustic waves that are generated by the initial light pulse.

To date, two main classes of detectors have been used. One class uses piezoelectric materials, which produce a voltage in response to stress from passing acoustic waves. The other class may be referred to as 'optical detectors', though this mainly refers to optical interferometers, of which the Fabry-Perot interferometer has so far been the focus. Both classes have associated advantages and disadvantages, and the exact form of the detector depends heavily on the particular set-up of the experiment.

It is necessary to clarify the term *Photoacoustic Imaging*. *PA Imaging* may refer to the production of one, two of three dimensional maps of optical absorbers, produced either through *Photoacoustic Tomography* (PAT), or *Photoacoustic Microscopy* (PAM). PAM generally uses a focused detector to measure the acoustic signal from a single point within an object. Measurements can be taken from a grid of points to form an image, and hence no reconstruction algorithm is necessary. PAT on the other hand typically has the capability to measure the propagated disturbance at all points across a detection surface simultaneously, however the image must then be reconstructed from this data. PAT is the favourable option for *in vivo* imaging, because of the potential for reduced acquisition times.

This project has focused on the development of a new type of detector for use in 3D PAT. The detection system is based on a Michelson interferometer, which has the possibility to overcome some of the limitations of other systems being developed.

The main goal of the project was to demonstrate that photoacoustic imaging was possible with the new detector. Quantitative measurements such as blood oxygenation saturation have been performed using photoacoustic imaging[8, 9], but such quantitative measurements were beyond the scope of this project.

Chapter 2

Photoacoustic Theory

Before any discussion can be had on the merits of different techniques involved in photoacoustic detection and imaging, it is important to briefly look at how photoacoustic waves are generated, and how they propagate. Material covered in this chapter summarises the considerations when designing, building, and testing, the final photoacoustic imaging system.

2.1 Photoacoustic Wave Generation

As mentioned, the photoacoustic effect is the production of acoustic waves as a result of an object absorbing some amount photon energy. The energy in the light is converted to heat energy, which results in thermoelastic expansion. Typical temperature increases are less than 0.1 K. This in turn radiates acoustic waves.

The source of the excitation light used to date has predominantly been Q-switched nanosecond pulsed lasers[10, 11, 12]. There has also been some work into using high power laser diodes running at higher repetition rates[13, 14], though these cannot yet match the pulse intensity of Q-switched lasers. Microwave excitation sources have also been used[4], though their use is limited to imaging of a few specific tissue types, and at lower resolution. For this reason, the signal generation processes described below will have an emphasis on high power, short pulse laser excitation methods.

2.1.1 Short Excitation Pulse Duration

As soon as an object starts being heated, it will begin to radiate away acoustic energy. For the purpose of detection and reconstruction, it is preferable that a PA wave is a single intense pulse. For this to occur, two conditions must be met, referred to as thermal, and stress confinement[15].

Thermal confinement is the condition that the excitation pulse time, t_p is less than the time it takes for a significant fraction of the heat to dissipate away. The distance that the heat will diffuse over the duration of the pulse is approximately given by the thermal diffusion length[4], $\delta_T = 2\sqrt{D_T t_p}$ where D_T is the thermal diffusivity of the object. For most soft tissues $D_T \approx 1.4 \times 10^{-3}$ $\mathrm{cm^2s^{-1}}$[16]. Even a relatively long excitation pulse time of $t_p \approx 500$ ns only results in $\delta_T = 0.5$ μm, which is much less than the expected resolution of most imaging systems. The condition of thermal confinement is therefore usually met.

Stress confinement is the condition that the generated acoustic wave has not propagated significantly outside the absorber during the excitation pulse time. The maximum allowable pulse time to satisfy this condition is therefore $t_p = L_p/c$, where L_p is the desired resolution and c is the local speed of sound. For a resolution of 150 μm, this corresponds to a pulse time of $t_p = 100$ ns. Therefore, stress confinement places a more stringent condition on excitation pulse duration.

The short pulse time produced from Q-switched lasers satisfy both thermal and stress confinement very well. These typically have pulse durations of 5 to 20 ns with peak powers up to tens of megawatts. While flashlamp pumped lasers offer higher peak powers, they have repetition rates limited to tens of hertz. Diode pumped Q-switched lasers however, offer repetition rates of up to 1 kHz[17], which is advantageous for reducing data collection times when signal averaging is required. Laser diodes have also been used as excitation sources directly[13], with the aim of reducing costs, and also exciting lower frequency acoustic waves (which have a larger penetration depth) by increasing exposure times. Pulse times of up to $\tau_p = 200$ ns have been tested, which do excite lower frequency waves. The reduced confinement produced by such long pulses however, significantly lowers peak acoustic pressure.

The increase in temperature (ΔT), due to the absorption of laser energy (under the condition of thermal and stress confinement) is given by:

$$\Delta T(\vec{x}) = \frac{F(\vec{x})\mu_a(\vec{x})}{c_p \rho} \tag{2.1}$$

where μ_a ($\mathrm{cm^{-1}}$) is the optical absorption coefficient (see Chap. 2.3), F ($\mathrm{Jcm^{-2}}$) is the local light fluence, c_p is the specific heat capacity, ρ is rest density, and $\vec{x}$ is the spatial variable.

The resulting thermal expansion of the irradiated area will result in an increase in pressure of p_0, given by[4, 18]:

$$p_0 = \Gamma \mu_a F \tag{2.2}$$

where Γ is known as the *Gruneisen* parameter. The Grunesian parameter is related to the thermal expansion coefficient β ($\mathrm{K^{-1}}$), the specific heat capacity C_p ($\mathrm{Jkg^{-1}K^{-1}}$), and the speed of sound c by $\Gamma = \beta c^2/C_p$. Γ is thermo-acoustic efficiency, effectively determining what proportion of absorbed light energy is converted to acoustic energy[12]. The increase in pressure, p_0, is interpreted as the peak acoustic pressure. If the excitation light is collimated and directed down the z axis say, the fluence can be written as decreasing exponentially with z as it is absorbed. In this situation (which is indicative of a laser excitation source), Eqn. 2.2 becomes:

$$p_0(z) = \Gamma \mu_a F_0 e^{-\mu_a z} \tag{2.3}$$

where F_0 is the initial light fluence[13]. This equation is an expression for the initial axial acoustic pressure generated by an infinitesimally short pulse.

2.1.2 Longer Excitation Pulse Duration

For excitation pulse durations which do not satisfy the thermal and stress confinement conditions, Eqn. 2.3 is no longer valid. It is useful to know the effect of longer pulse durations since all pulse durations are finite in reality. The effect of long pulse duration depends on the geometry of the system and so must be modelled numerically. It has been shown[13, 19] that the PA signal at the detector $P_f(\vec{x}, t)$ is a convolution of the pressure signal initially produced from an impulse, $p(\vec{x}, t)$ and the laser temporal profile $g(t)$:

$$P_f(\vec{x}, t) = g(t) * p(\vec{x}, t). \tag{2.4}$$

2.2 Acoustic Wave Propagation in Tissue

Ultrasound, like all acoustic waves, is the propagation of a mechanical wave through a material. In solids, there are three possible modes of acoustic waves: one longitudinal and two transverse (or shear). Liquids and gasses have almost no ability to transmit shear waves, due to the non rigid nature of inter particle bonds. Biological soft tissues generally fall into the 'liquid' category, and so shear waves may reasonably be neglected in the remainder of this discussion.

2.2.1 Descriptions of Acoustic Waves

To describe the longitudinal component of an acoustic wave, many quantities may be used. Typically, the 'amplitude' of an acoustic wave is given by acoustic pressure p, however it may also be described by sound intensity I, the particle velocity v, the particle displacement ξ, and the velocity potential ϕ. While acoustic pressure p will predominantly be used when discussing acoustic waves, the other measures are useful descriptions in certain situations. Particle displacement for instance is of interest when considering acoustic detection, since it is the movement of particles, rather than changes in pressure that are usually detected, as will be seen in Sec. 4.1. Assuming the acoustic pressure is not so large as to cause non-linear effects, it is related to particle displacement by:

$$p(\vec{x}, t) = -E \frac{\partial \xi(\vec{x}, t)}{\partial \vec{x}} \tag{2.5}$$

where $\vec{x}$ is the spatial coordinate, and E is the appropriate modulus of elasticity for the medium[20]. The negative in Eqn. 2.5 is due to the convention of the sign of pressure. ξ may be found in terms of p by integration, and the spatial coordinate can be replaced by a temporal one by using the relationship for the speed of sound c:

$$c = \frac{dx}{dt}. \tag{2.6}$$

Given that particle displacement is often the detected quantity, it is useful to understand how it varies with wave frequency ν. Rewriting Eqn. 2.5 in its integral form, Eqn. 2.6 can be used to change the integration variable. We can then make use of the relation between wavespeed and elastic modulus: $c = \sqrt{E/\rho}$, as well and use the expression for acoustic impedence, z to give:

$$\xi(\vec{x},t) = \frac{-1}{z}\int p(\vec{x},t)dt \tag{2.7}$$

The frequency dependence can be shown by substituting a pressure plane wave, $p = p_0 sin(kx-\omega t)$ into Eqn. 2.7, along with the relation between frequency and angular frequency: $\omega = 2\pi\nu$. The resulting relation is:

$$\xi(\vec{x},t) = \frac{p_0}{2\pi z\nu}cos(kx-\omega t) \tag{2.8}$$

where the negative has been excluded to define positive displacement as displacement in the direction of travel.

The important relationship to note here is that the amplitude of the particle displacement is inversely proportional to frequency. This means that for a given acoustic pressure, higher frequency waves will result in a lower particle displacement, and so may be more difficult to detect where the detection mechanism is based on particle displacement.

The velocity potential ϕ is a quantity used in fluid dynimics and is the gradient of the flow velocity. It is mentioned here because it is often used as a mathematical convenience in reconstruction algorithms as will be seen in Chap. 3. It is related to pressure by:

$$p(\vec{x},t) = -\rho\frac{\partial\phi(\vec{x},t)}{\partial t} \tag{2.9}$$

where ρ is the (undisturbed) density of the medium[21].

Finally, it is worth noting the relationship between acoustic *intensity*, I, and acoustic *pressure* is:

$$I \propto p^2. \tag{2.10}$$

Acoustic intensity is the energy in the sound wave per unit time per unit area. This is useful to note because energy is a conserved quantity, while pressure is not.

2.2.2 The Wave Equation in Photoacoustics

For the purposes of numerical modelling, and understanding procedures of tomographic inversion, it is necessary to briefly describe the evolution of a PA disturbance. A pressure distribution $p(\vec{x},t)$ (which is the deviation from rest pressure) that is generated by a laser pulse, is described by the homogeneous wave equation, 2.11, along with initial conditions 2.12 & 2.13 [22, 23, 24]:

$$\frac{\partial^2 p(\vec{x},t)}{\partial t^2} = c^2 \nabla^2 p(\vec{x},t) \tag{2.11}$$

$$p(\vec{x},0) = p_0(\vec{x}) \tag{2.12}$$

$$\frac{\partial p(\vec{x},0)}{\partial t} = 0. \tag{2.13}$$

This form of the wave equation is easily solved numerically, and was used in simulations as will be discussed in Chap. 3. The system is equivalently described by the inhomogeneous wave equation[13, 21]:

$$\frac{\partial^2 p(\vec{x},t)}{\partial t^2} - c^2 \nabla^2 p(\vec{x},t) = \frac{\partial}{\partial t} p_0(\vec{x}) \delta(t) \tag{2.14}$$

where the RHS is effectively the source term. The Dirac delta ensures that the source is only 'on' during the laser pulse (which has been assumed to be infinitesimally short).

2.3 Optical and Acoustic Properties of Tissue

No method of soft tissue imaging is intrinsically better than any other, however it has been shown that the scattering and absorption properties (both optical and acoustic) of biological tissue, lend themselves to the utilisation of a hybrid optical/acoustic technique[25]. This set of tissue properties also influences the design and operation of any PA imaging device. For this reason, a summary of optical and acoustic properties has been collected for a range of materials which may find their way into any PA imaging system.

2.3.1 Optical Absorption and Scattering Properties

While optical scattering and absorption are complex processes, in PA systems the main consequence of interest is the total attenuation of the excitation pulse. Assuming the incident light is collimated and of 'large' lateral extent (such as an expanded laser beam), the intensity I, at a distance z into a homogeneous medium is given by:

$$I(z) = I_0 e^{-\mu_t z} \tag{2.15}$$

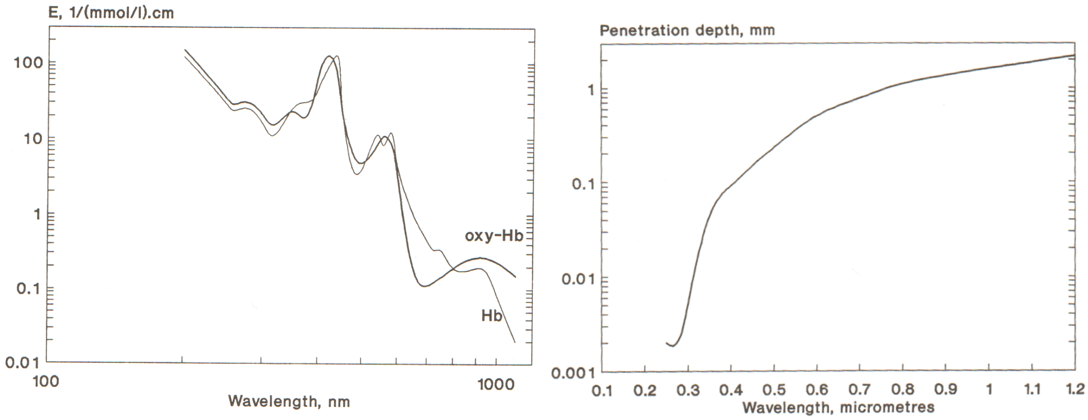

(a) (b)

Figure 2.1: (a) shows the absorption of light as a function of wavelength for oxygenated, and deoxygenated haemoglobin. The vertical scale is the absorption coefficient per unit concentration of Hb. (b) shows the penetration depth of light in caucasian skin. Penetration depth is the reciprocal of the attenuation coefficient, ie. $1/\mu_t$. Image taken from [16].

where I_0 is the intensity at $z = 0$[26]. The condition of homogeneity can be eased if the equation is applied recursively at the boundary of any two different media. When attenuation is dominated by absorption, the total attenuation coefficient, μ_t is :

$$\mu_t = \mu_a + \mu_s \tag{2.16}$$

where μ_a and μ_s are the absorption and scattering coefficients respectively. When scattering is the dominant effect, the attenuation coefficient must be modified to:

$$\mu_t = \sqrt{3\mu_a(\mu_s' + \mu_a)} \tag{2.17}$$

where μ_s' is the reduced scattering coefficient, which is related to the scattering coefficient by $\mu_s' = (1-g)\mu_s$. g is the scattering anisotropy parameter, which is the mean cosine of the scattering angle.

Understanding scattering is important in photoacoustics, because it determines how the excitation laser fulence changes at different depths in tissue. Understanding absorption is important because it determines the amplitude of the initial pressure distribution caused by the excitation laser.

Both scattering and absorption are wavelength dependent properties. It would be ideal to find a wavelength where the object in question (eg. blood) absorbed strongly, and the surrounding medium (eg. skin) attenuated only weakly. Unfortunately, wavelengths which are highly absorbed are also generally scattered more, and hence have a lower penetration depth. An example of the trade off between absorption and attenuation due to scattering may be seen in Fig. 2.1.

In practice, the 'optimum' wavelength will depend on the absorption and scattering properties of all components present, as well as the required imaging depth. Other considerations include the ability to generate a short intense laser pulse at a given wavelength. For imaging blood vessels without preference to oxy or de-oxy haemoglobin (Hb), $\lambda \approx 800 - 900$ nm excitation light generally satisfies all criteria relatively well. However, 1064nm light produced from Q-switched Nd:YAG lasers is generally considered acceptable, since high intensities are readily produced [27, 12, 28]. This was the laser type which was available for use in this project. As such, scattering and absorption coefficients for a variety of media at $\lambda = 1064$ nm are given in Table 2.1. It should be noted that the figures shown may vary significantly depending on the exact tissue specimen in question. Values which are not shown either could not be found, were not relevant or could be calculated from other parameters already present.

Table 2.1: Optical attenuation coefficients at $\lambda = 1064$ nm

Medium	$\mu_a(\mathrm{cm}^{-1})$	$\mu_s(\mathrm{cm}^{-1})$	$\mu_s'(\mathrm{cm}^{-1})$	g
water[29]	0.2	≈ 0	-	-
oxy-Hb (Ht=0.4)[26]	3	-	3.4	≈ 0.99
Hb (Ht=0.4)[26]	0.3	-	6.6	≈ 0.99
caucasian skin[26]	0.16	-	17.11	-
subcutaneous fat[26]	0.07	-	1.69	0.8
white brain matter[26]	0.4	110	-	0.95
skull[26, 30]	0.16	-	15.92	0.95
India ink[26]	$(36 \pm 4)/\%$	$(4.6 \pm 2.0)/\%$	-	0.30 ± 0.18
Intralipid 10%[26]	$(0.054 \pm 0.02)/\%$	$(1.30 \pm 0.05)/\%$	-	0.50

Considerable testing and optimisation on tissue phantoms is always conducted before trials of *in vivo* imaging take place. In photoacoustic imaging, two materials are used ubiquitously to simulate optical absorption and scattering in tissue. India ink is used as an optical absorber, because it is absorbed over a large frequency range, and has similar acoustic properties to blood[31, 32]. *Intralipid 10%* is used as a propagation medium, since it is of similar make up to real soft tissue (water and oils)[33, 34, 35]. Both substances can be diluted to simulate correct optical absorption/scattering properties, and were used in this project to create 'realistic' phantoms. Their absorption and scattering coefficients are given in Table 2.1 as quantities per percent concentration.

Maximum Permissible Exposure

It is important to note that there is a maximum permissible exposure (MPE) to laser radiation. For nanosecond pulsed IR laser light, such as produced from a Q-switched Nd:YAG laser, the MPE to human skin is 30 mJ/cm^2 per pulse. This MPE is based on 100 pulse repetitions, where the illumination is over an area of not more than 10 cm^2. These limits were adhered to in all PA measurements taken in this project. Full conditions for calculating MPE can be found in

[36].

2.3.2 Acoustic Absorption and Scattering Properties

Acoustic waves are also attenuated as they travel. Both absorption and scattering contribute to this attenuation, which results in a lower amplitude signal at the detector. Scattering also increases the production of artefacts in all ultrasound imaging, however this effect is reduced in PA imaging, because the sound only needs to propagate from source to detector, rather than the two way trip needed in traditional ultrasound.

Reflections from material boundaries may also be considered a sort of scattering, but this will be considered in Sec. 2.3.3. The acoustic attenuation of a plane wave, travelling through a homogeneous medium is given by:

$$I(z) = I_0 e^{-2\alpha z} \tag{2.18}$$

where I_0 is the initial acoustic *intensity*, z is the propagation distance, and $\alpha(\mathrm{Np\ cm^{-1}})$ is the frequency dependent attenuation constant. Due to relationship between acoustic intensity and pressure in Eqn. 2.10, Eqn. 2.18 can be rewritten:

$$p(z) = p_0 e^{-\alpha z} \tag{2.19}$$

where p_0 is initial acoustic pressure[37]. Some values of acoustic attenuation coefficients are shown in Table 2.2. These represent a sample of materials which a PA signal may have to traverse during propagation from source to detector.

Table 2.2: Acoustic attenuation coefficients for ultrasound frequencies

Medium	$\alpha(\mathrm{Np\ cm^{-1}})$	Frequency Range ν (MHz)
water[38]	$2.53\nu^2 \times 10^{-16}$	3-70
fused silica[39]	$2.6\nu^2 \times 10^{-22}$	1-10
polystyrene[40]	$4.6\nu^{1.4} \times 10^{-9}$	0.02-0.2
PMMA[1][40]	$0.054 log_{10}\nu - 0.242$	0.02-0.2
blood (Ht=0.4)[16]	$(2.4, 6.1, 22.1, 30) \times 10^{-2}$	1, 2.4, 4.6, 10
brain[16]	$(6.9, 9.5, 51) \times 10^{-2}$	1, 2.2, 5
skin[16]	$0.4, 1.06$	1, 5
subcutaneous fat (pig)[16]	$0.21, 0.07, 0.56$	1, 1.6, 6
skull[16]	$1.51, 2.5, 9$	0.8, 1, 3

[1]Poly(methyl methacrylate)

2.3.3 Acoustic Impedance

As mentioned, reflections off boundaries between two media will also attenuate forward propagating ultrasound. The amount of reflection is determined by the relative (specific) acoustic impedances z, of the two media. The acoustic impedance of a material is given by the product of its density ρ, and its speed of sound c[20]:

$$z = \rho c. \tag{2.20}$$

The proportion of acoustic *energy* transmitted and reflected, T_e & R_e, as an acoustic wave travels from a medium of $z = z_1$ to a medium of $z = z_2$, is given by the transmission and reflection coefficients[41]:

$$\begin{aligned} T_e &= 1 - R_e \\ R_e &= (\frac{z_1 - z_2}{z_1 + z_2})^2. \end{aligned} \tag{2.21}$$

The energy reflection and transmission coefficients correspond to the total acoustic *energy* reflected and transmitted, but it is useful to note that the acoustic *pressure* of the wave is transmitted and reflected differently. The pressure transmission and reflection coefficients, T_p & R_p, are given by[41]:

$$\begin{aligned} T_p &= \frac{2z_2}{z_1 + z_2} \\ R_p &= \frac{z_2 - z_1}{z_2 + z_1}. \end{aligned} \tag{2.22}$$

In this way, it is possible for the transmitted wave to have a greater acoustic pressure than the incident wave. Equations 2.21 & 2.22 are useful, because they allow design of efficient acoustic detection systems. This has led to the development of some optical detectors made from polymers rather than glass[27, 42], since polymers are typically more closely impedance matched to tissue. This is preferable because it allows a larger fraction of the acoustic energy to couple into the detector, which generally increases signal strength. The acoustic impedance for a range of materials which are often involved in photoacoustic techniques are shown in Table 2.3.

Table 2.3: Specific acoustic impedances

Medium	$c(\mathrm{ms}^{-1})$	$\rho(\mathrm{kgm}^{-3})$	Specific Impedance, z ($\mathrm{kgm}^{-2}\mathrm{s}^{-1}$)
water[38]	1480	1000	1.5×10^6
polystyrene[40]	1620	1031	1.67×10^6
polyethylene[38]	2000	920	1.8×10^6
PMMA[40]	2350	1168	2.74×10^6
glass[39]	4600	2800	13.1×10^6
whole blood[16]	1534	1055	1.61×10^6
brain[16]	1562	1041	1.62×10^6
fat[16]	1476	928	1.37×10^6
skull[16]	2700	1610	4.35×10^6

Chapter 3

Simulation and Image Reconstruction

Once the pressure distribution of the propagated PA wave has been detected at the surface, it is possible to mathematically reconstruct the initial pressure distribution. Many reconstruction algorithms exist for photoacoustic tomography, for many detector geometries. The detection system in this project consisted of a planar type detector (see Sec. 4.2), so the discussion of the reconstruction is limited to this geometry. *Köstli et al.*[21] detail a theoretically exact reconstruction algorithm for a planar detection geometry, which was the algorithm employed in this project. It is described only briefly here, for a rigorous derivation the reader is referred to the original article.

The methods detailed in Ref. [21] were also the basis for simulation of the forward propagation. Both the forward and inverse algorithms rely on being able to write the pressure distribution as a Fourier transform. As a computational convenience, it was useful to consider the velocity potential rather than the acoustic pressure. It is irrelevant whether the detected quantity is pressure, velocity potential, or particle displacement (as was the case in this project), as conversion between these quantities can be performed using the relations given in Sec. 2.2.1.

3.1 Simulation of Acoustic Propagation

All simulations performed in this project relied on a simple algorithm for solving the wave equation numerically. In fact, conventional PDE solving was not required, because the problem can be solved pseudo-analytically. Fourier transforming the initial pressure distribution $p_0(\vec{x})$, gives $P(\vec{k})$. Since plane waves are also analytic solutions to the wave equation, they are propagated through time simply by adding phase. The real space pressure field at the new time can then be recovered by inverse Fourier transforming. The whole process is neatly presented as follows:

$$p(\vec{x},t) = \frac{1}{(2\pi)^3} \iiint P(\vec{k}) cos(\omega t) e^{i\vec{k}\vec{x}} d^3\vec{k} \tag{3.1}$$

$$P(\vec{k}) = \iiint p_0(\vec{x}) e^{-i\vec{k}\vec{x}} d^3\vec{x}. \tag{3.2}$$

This algorithm was implemented in MATLAB, where the Fourier transforms were replaced by their discrete versions (FFT in this case).

3.1.1 Validation of Correct Forward Implementation

In order to insure that the algorithm had been implemented correctly, the first 'simulation' was a direct recreation of the example presented in the literature[21]. An initial pressure distribution was laid out on a $64 \times 64 \times 32$ point grid, where the dimensions are in the x, y, and z directions respectively. The initial pressure was distributed over a 3×3 grid, and the peak was set to unity. An (x, y) slice is shown in Fig. 3.1. A comparison between these figures show that the original and reproduced implementation of the forward algorithm is identical, which verifies that further simulations are reliable. Plots 3.1 (c) & (d) show a slice at a fixed y value as the pressure passes through the plane at $z = 0$.

3.1.2 Simulation of a Real Phantom

The forward simulation was important for two reasons. Firstly, it allowed validation of the reconstruction algorithm, as will be discussed in Sec. 3.2. Secondly, it guided apparatus development by allowing a comparison between experimental data and theory. This was particularly the case when the very first measurements were taken, as the detected signal looked nothing like the expected signal (see Sec. 5.2). Such a comparison is shown in Fig. 3.2. The detected pulse was produced from an ink filled silicone tube of internal diameter 500 μm, placed 3.2 mm from the mirror (directly in front of the mirror position being interrogated). The diluted ink had an absorption coefficient of $\mu_a \approx 36$ cm^{-1}, and the propagation medium was water. The illumination fluence was ≈ 30 mJcm^{-2}, and the sensing mirror substrate was a 150 μm thick glass microscope coverslip (see Sec. 5.3). The simulation was set up to match these parameters as closely as possible. The pressure at the absorber was calculated from Eqn. 2.2, and the transmitted pressure and displacement were calculated using the relationships described in Sec. 2.2.1. Note that in the simulation, it is the *pressure* which is propagated, and the *displacement* is calculated after. The reverse is true for the experimental data. The Michelson system detects particle displacement, and it is the pressure which must be calculated afterwards.

A comparison between the simulated and detected pressure/displacement in Fig. 3.2 shows reasonable agreement. It can be seen that the acoustic amplitude after propagation relies fairly heavily on the type of initial conditions used. While the 'smoothed top hat' initial conditions

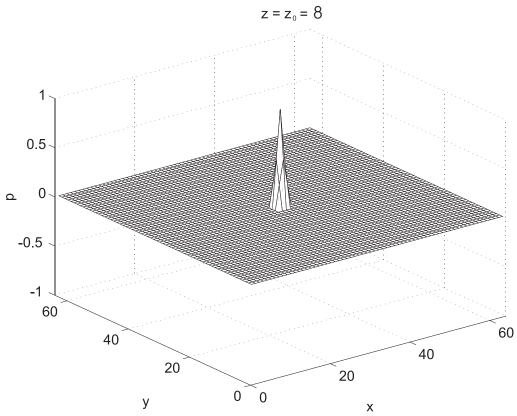

(a) Initial pressure distribution - original.

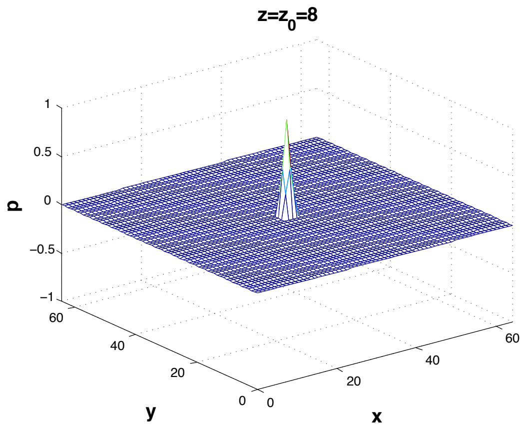

(b) Initial pressure distribution - reproduction.

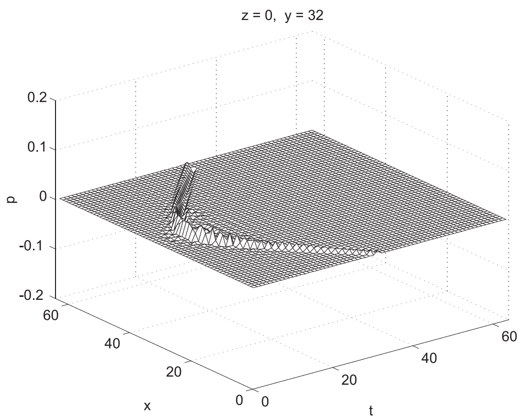

(c) Propagated pressure distribution - original.

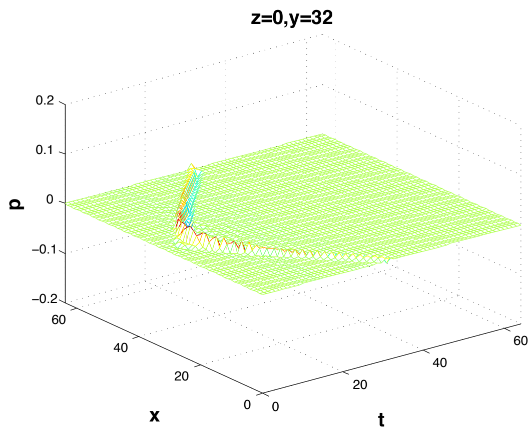

(d) Propagated pressure distribution - reproduction.

Figure 3.1: (a) shows the initial pressure distribution from *Köstli et al.*[21]. (b) shows the distribution from the implementation used in this project. The two are identical. (c) & (d) show original and reproduced simulated propagated acoustic wave. Again, they are identical.

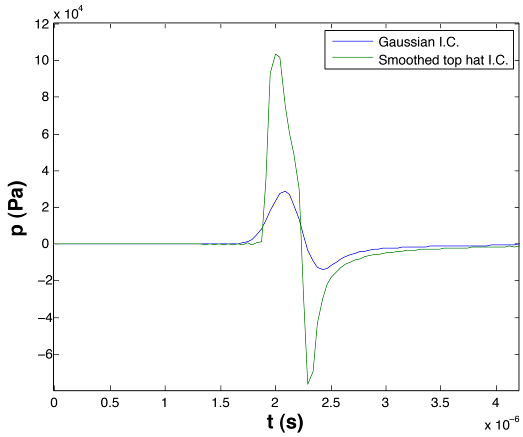

(a) Simulated pressure.

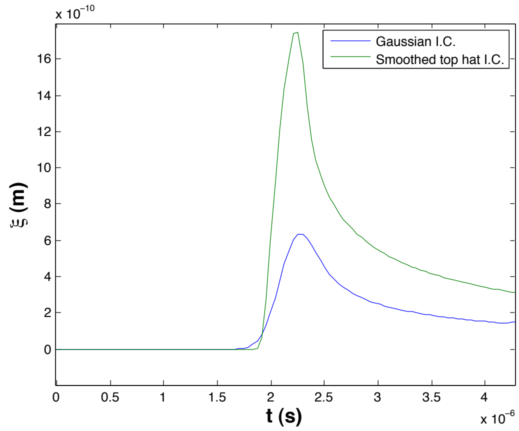

(b) Simulated displacement.

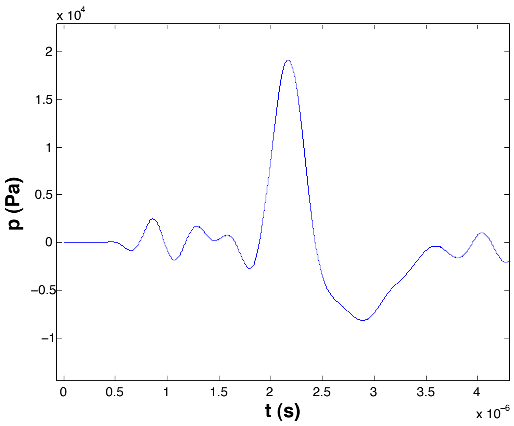

(c) Detected pressure.

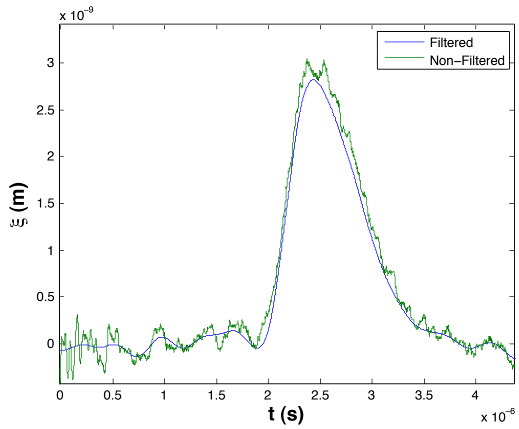

(d) Detected displacement.

Figure 3.2: A comparison between simulation and experimental data. It can be seen that there is a significant discrepancy in frequency, which is the likely cause of the differing amplitudes. Qualitatively however, there is good agreement.

(I.C.) better represents the geometry of a cross section absorbance profile, the gaussian I.C. was more smoothly propagated (due to its less discontinuous nature).

The discrepancy in the acoustic amplitudes are likely due to the difference in the frequency of the simulated and detected wave. This was probably caused by not taking into account the acoustic properties of the silicon tube. It is possible that the tube caused the pressure wave to propagate as though the diameter of the initial disturbance was larger than it actually was. Keeping this in mind, much of the qualitative behaviour matches relatively well, such as the negative pressure component having a lower magnitude than the positive component.

Such a simulation was used to determine the feasibility of using a Michelson interferometer as a photoacoustic sensor. When considering Eqn. 4.9, the intensity modulation from the simulated wave is predicted to be $\approx 0.15\%$. This level of modulation was considered sufficiently large to detect, on the basis of known photodiode signal detection capabilities.

3.2 Tomographic Reconstruction of the Initial Pressure Distribution

This method provides a theoretically exact reconstruction of the initial pressure distribution $p(\vec{x}, t = 0)$, where pressure measurements are known for all times $t > 0$ on the infinite (x, y) plane: $p(x, y, z = 0, t)$. Firstly, a 2D Fourier transform is taken at the plane $z = 0$ for every time $t > 0$:

$$A(k_x, k_y, t) = \iint_{-\infty}^{\infty} p(x, y, z = 0, t) e^{-i(k_x x + k_y y)} dx dy. \tag{3.3}$$

Taking the cosine transform of Eqn. 3.3 with respect to time, gives the Fourier transform of the pressure:

$$P(\vec{k}) = \frac{c k_z}{\sqrt{k_x^2 + k_y^2 + k_z^2}} \int_0^{\infty} A(k_x, k_y, t) cos(\omega t) dt \tag{3.4}$$

where $\omega = c\sqrt{k_x^2 + k_y^2 + k_z^2}$. The pressure distribution at $t = 0$ can then be found by taking the 3D inverse Fourier transform of Eqn. 3.4:

$$p(\vec{x}, t = 0) = \frac{1}{(2\pi)^3} \iiint_{-\infty}^{\infty} P(\vec{k}) e^{i(k_x x + k_y y + k_z z)} dk_x dk_y dk_z. \tag{3.5}$$

In any real situation, pressure measurements can only be made over a finite plane, over a finite time interval. This makes the reconstruction non-exact, as does the necessity to use discrete transforms. Some of the assumptions used in the derivation put a limit on the depth for which the reconstruction is valid. For a detection surface of dimensions $L \times L$, the greatest depth of a source which can be reconstructed is $L/2$. This corresponds to limiting the detection interval to $0 \le t \le L/2c$.

This algorithm has been used to reconstruct PA images taken of the vascular structure of a mouse brain, and a human palm[43]. Despite its successful application, it has the drawback of needing a relatively large number of temporal measurement,. i.e. the number of measurements taken of the (x, y) surface between $t = 0$ and $t = L/2c$ should be large. This is because the discrete cosine transform must be carried out in time, so the size of the temporal measurement intervals is just as important as the spatial intervals.

3.2.1 Implementation of the Inverse Algorithm

The implementation of the inverse algorithm proved substantially more problematic than the forward one. In fact, the algorithm could not be made to operate in an identical manner to that of Ref. [21], and the results achieved ended up being of slightly lower quality, though still acceptable. A comparison between results produced by the original implementation and those from this project may be seen in Fig. 3.3.

The non-exact reconstruction of the original pressure distribution by the original implementation is a result of taking data only from a finite plane, for a finite time. The goal was to simply reproduce this level of accuracy. However, it can be seen in Fig. 3.3, that the implementation used in this project produces significantly different results. Firstly, the magnitude of the reconstructed pressure distribution is several times what it should have been. Secondly, the distribution has been spread out more than it should have been, especially in the x, y plane. Finally, there is significant oscillation present in the reproduction, which was not present in the original implementation. It should be noted that the symmetrical appearance of the 'z-cut' in the z direction is as a result of assumptions used in the algorithm. The reconstruction is valid for only half the depth shown, and as such, the deeper half should be ignored.

The reconstruction is essentially a three step process, with the first and third steps simply being two and three dimensional Fourier transforms respectively (which can be substituted by one line of code using a FFT). The error in implementation was therefore certainly due to the translation of Eqn. 3.4 into code. Indeed, while the original paper stated that "the infinite integrals [were replaced] by the FFT algorithm", the reconstruction could not be made to work using this method. Instead, the integral was evaluated manually, by taking the product of the two terms enclosed, then integrating in the time direction (for every k_x, k_y, k_z point). There were other subtleties in the implementation which were not explicitly described in the original paper, and the method by which these were implemented may have contributed to the non-exact reproduction.

In addition to the discrepancy shown by the example in Fig. 3.3, there was also a problem when real data was to be reconstructed. When real length, time, and wave speed values were used in the algorithm, it ceased to function correctly. Using real units, objects were reconstructed

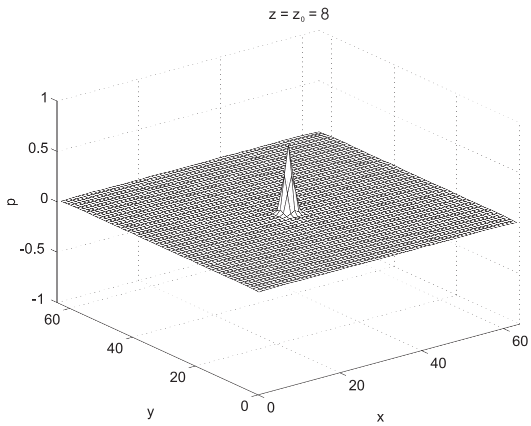

(a) Original implementation - xy slice

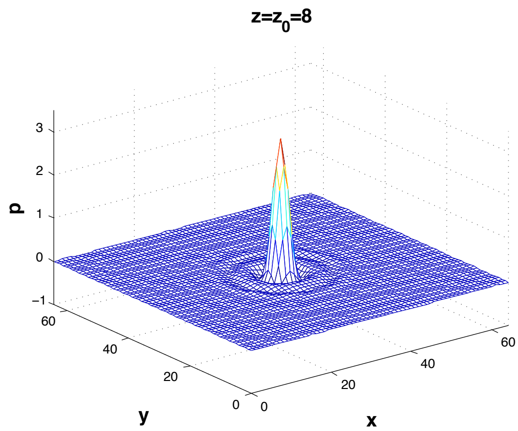

(b) Reproduced implementation - xy slice

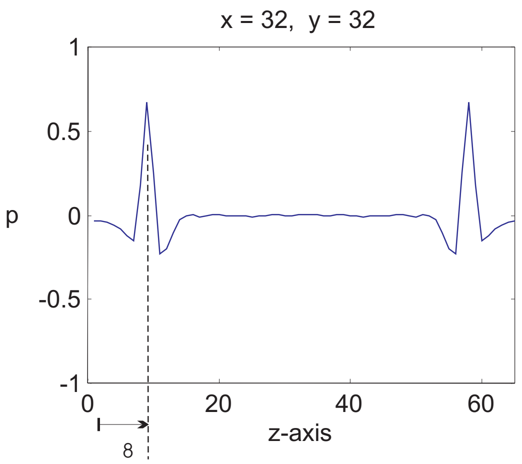

(c) Original implementation - z cut

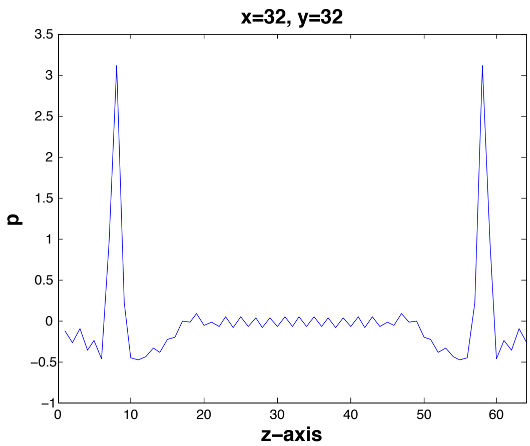

(d) Reproduced implementation - z cut

Figure 3.3: The above images show reconstructed images of the initial conditions shown in Fig. 3.2. The original implementation more accurately reproduces the initial pressure distribution than the reproduction, however they are qualitatively similar. (a) & (c) taken from Ref. [21].

to the correct z-depth, however they were highly spread out in the x, y directions. In fact, using quantities applicable to this project, any disturbance that was propagated from $z = z_0$, be it a point or a cylinder, was reconstructed to a plane taking up the whole x, y space, centred around z_0. While this strange behaviour certainly indicated that the algorithm was not functioning as intended, it was relatively easy to fix. Simply nondimentionalising the quantities made the reconstruction function as intended (apart from the discrepancy in magnitude and oscillations as mentioned). Nondimensionalisation sets the spacing of the spatial and temporal points to unity. This is described by the equations:

$$\begin{aligned} x^* &= \frac{x}{\Delta x} \\ y^* &= \frac{y}{\Delta y} \\ z^* &= \frac{z}{\Delta z} \\ t^* &= \frac{t}{\Delta t} \\ c^* &= 1 \end{aligned} \tag{3.6}$$

where Δ indicates the spacing between points in real dimensions, and the $(^*)$ denotes the nondimentionalised coordinated. In practice this is easy to implement. When the reconstruction requires time or space vectors, they are simply given as a list of integers, instead of the actual spatial or temporal quantities, such as metres or seconds. Redimensionalisation is also trivially achieved by substituting the original time and spatial vectors post reconstruction.

Chapter 4

Photoacoustic Detectors

The diverse range of applications for biomedical photoacoustics has led to the production of many different types of detectors, in many different geometries. In general, it is desirable that any photoacoustic detection system satisfy three main criteria: high resolution, high sensitivity and short data acquisition times. As will be shown in this chapter, all existing detectors have limitations in at least one of these areas, which provides motivation for the development of the new detection system on which this project is based.

4.1 Existing Detectors

There are two general *modes* of photoacoustic signal detection: forward and backward. In forward mode, tissue is illuminated by the excitation laser on one side, and the generated PA signal is detected on the other. This mode is suitable only when the tissue sample is sufficiently thin that light and the ultrasound it produces can propagate through the entire thickness of the sample without undue attenuation, suggested applications may include breast cancer screening[7]. Backward mode imaging involves the ultrasound detector being on the same side as the illumination source. This has the advantage that there is a high laser fluence close to the detector, which results in stronger PA signals being detected, and improved resolution. The difficulty of backward mode imaging is that the detector shadows the region immediately beneath it. To get around this, light may be shone from beside the detector, between pixel elements, or the whole detector may be made transparent to the excitation wavelength. The former option is used when the detector is made form piezoelectric 'pixels', as these are usually opaque. Transparent detectors have been made based on the Fabry-Perot interferometer. Though piezoelectric based detectors are commercially more advanced, there is as yet no consensus about the 'best' detection method, which may well depend on the exact imaging situation.

4.1.1 Piezoelectric Arrays

Piezoelectric materials offer an obvious choice for ultrasound detectors. As the pressure wave passes through the material, the stress causes a mechanical deformation, which induces an electric charge on both electrodes. Only a small strain is required to produce a large voltage ($\approx 100\ nV/Pa$ of acoustic pressure, depending on frequency[44]), making them very sensitive to acoustic waves. To create a piezoelectric detector, many individual elements may be formed into arrays[44]. This has the advantage that the detector may have an arc, or bowl geometry (used for PA microscopy), and that the size of the detector may be extended simply by adding more pixels. There is however a difficulty in creating sufficiently small elements, which can limit lateral resolution (however resolutions of 200 μm have been reported at imaging depths of up to 6 mm[45]). Acoustic coupling into the high impedance piezoceramic materials had been an issue, though this has largely been remedied by the use of polymeric piezoelectric materials such as PVDF[12]. As mentioned, a major disadvantage of piezoelectric based materials is their shadowing of the tissue from the excitation light. Is has been shown that new classes of coated PVDF can be made optically transparent for PA purposes, though these are still in the early development stages[46]. In addition, piezoelectric based detectors have been combined with standard reflection based ultrasound, to create hybrid systems which potentially provide more information to the operator.

4.1.2 Fabry-Perot Interferometers

Fabry-Perot (FP) based photoacoustic detectors are the most developed of the detectors which use a simple plane-detection geometry. They have been used to create *in vivo* 3D images of vascular structure in mouse brains (through the skull) to a depth of 4 mm[34], and to a depth of 6 mm in a human palm[43]. The Fabry-Perot cavity is typically a thin polymer film on the order of tens of microns wide, with a reflective coating on both sides. This is in turn bonded to a thick polymer substrate. Dielectric coatings typically form the mirrors, which allow the excitation wavelength through, while providing high reflectivity at the interrogating wavelength. Ultrasound is detected by monitoring the slight variations of the cavity length in the axial direction, caused as pressure waves pass through. In this respect it is the *particle displacement* which is detected, rather than the acoustic pressure. Changing the length of the FP cavity varies the intensity of reflected light. The variation in reflected intensity for a given variation in thickness is non-linear, being of the form of an airy function[47]. The *finesse*, F of the cavity (which is determined by the reflectivity of the mirrors), determines the peak sensitivity of the interferometer. Cavity finesses of up to $F = 42.2$ have been achieved in these forms of PA detectors[27]. The intensity response function for a FP cavity of $F = 42.2$ can be seen in Fig. 4.1.

This affords the FP detector very high sensitivity in some regions (similar to that of piezo detectors), but in others, even a relatively large change in cavity length has little effect on the reflected intensity. For this reason, the probing laser must constantly be tuned to keep the wavelength in the regime where the cavity is at its most sensitive. This greatly increases the complexity of the system. In addition, it eliminates the possibility of taking measurements over the whole plane of view simultaneously, since slight variations in manufactured cavity length over the surface mean the sensitivity is not the uniform everywhere. In fact, the cavities created so far vary in width by several wavelengths of light over their surface.

The solution to this has been to bias the sensitivity to a maximum at each on the cavity one at a time, building up a 2D scan by rastering over the surface. Given that signal averaging is usually required, and flashlamp pumped Q-switched lasers usually only operate at 10Hz, this drastically increases data acquisition times. Acquisition times could be reduced by using a diode pumped laser. However increasing the number of pulse repetitions decreases the MPE of each pulse, and hence decreases the amplitude of the PA wave.

4.1.3 2D Optical Reflectance Based Detector

Another detector which can overcome problems associated with both the piezoelectric and Fabry-Perot based detectors, is based on variable optical reflectance at the interface of two media. In this design, the ultrasound sensor is a trapezoidal prism, with the largest surface in contact with the area to be imaged[48, 49]. An expanded interrogation laser beam is shone through the prism so that it reflects off this surface at close to the critical angle. The reflected beam is aimed at a CCD, which records the reflected intensity across the whole prism surface simultaneously. As an ultrasound wave reaches the prism, it compresses (or expands) the adjoining medium. This slightly increases (or decreases) the optical refractive index in this medium. Since the amount of reflected light from the prism surface is dependent on the relative refractive indices, the CCD captures a grayscale image of the instantaneous pressure distribution at the interface.

This setup is advantageous for two reasons. Firstly, the ability to capture the whole 2D pressure distribution simultaneously allows for significantly reduced acquisition times as compared to the Fabry-Perot detector. The small element sizes of typical CCD pixels also make the method intrinsically high resolution. Secondly, the prism is transparent, so the excitation laser may be shone through the detection surface, resulting in high laser fluence at the region of interest.

As will be shown in the next section, the detector developed in this project shares both these advantages. It is therefore interesting to investigate the important feature, of sensitivity. It is difficult to make direct comparisons of the between the sensitivity of detectors based on different mechanisms. However, for ‘optical’ based detectors, the sensitivity, S may be defined as the proportion of optical intensity modulation per unit acoustic pressure:

$$S = \frac{1}{R_{0,opt}} \frac{dR_{opt}}{dp} \tag{4.1}$$

where R_{opt}, is the optical reflectance (the subscript 0 indicates reflectance at ambient pressure), and dp is the change in pressure. For this detection system, it was said that the sensitivity is "between 0.19% and 0.81% gray level modulation per bar"[48], and this is seemingly independent of acoustic frequency.

Further comparisons to this detector design are made in the next section, where the system built in this project is detailed.

4.2 A New Detector Based on a Michelson Interferometer

The photoacoustic detection system created in this project was based on a Michelson Interferometer (MI). The basic premiss behind the ultrasound sensor is to propagate the acoustic waves through one of the interferometer mirrors. The particle displacement associated with the acoustic wave slightly changes the position of the mirror, resulting in some modulation of the interference intensity. A schematic of the Michelson sensor can be seen in Fig. 4.2 (the additional complexity of which will be discussed in Sec. 4.2.1). The output intensity of a standard MI is sinusoidal:

$$I = I_0 \frac{cos(\phi) + 1}{2} \tag{4.2}$$

where ϕ is the difference in 'phase' between the laser beams on their return trips down both arms, and I_0 is the maximum intensity. Moving the 'sensing mirror' by a distance ξ changes the phase by:

$$\phi = \frac{4\pi n\xi}{\lambda} \tag{4.3}$$

where n is the refractive index of the mirror substrate, and λ is the wavelength of the probing laser used. Note that the refractive index is only required where the substrate itself is distorted by the wave, and the mirror surface is on the 'back' of the substrate (in contact with the area being imaged). In the case that the whole mirror is simply repositioned, n is taken to be the refractive index of the surrounding medium (≈ 1 for air). Several different 'sensing mirror' configurations were investigated in this experiment, which are discussed in detail in Chap. 5.2.

Since the ultrasound wave passes through the mirror surface, the mirror movement and the particle displacement may be taken to be equal. The difference in phase between the two arms is also affected by the slight change in refractive index of the mirror substrate caused by acoustic compression (again assuming the mirrored surface is on the back of the substrate). However the change is negligibly small compared with that caused by the change in mirror position. A comparison between the sensitivities of a FP (Fabry-Perot) sensor and an MI sensor can be seen by comparing the output intensity functions shown in Fig. 4.1. While the FP detector appears to be much more sensitive to a change in phase, a direct comparison in this manner is

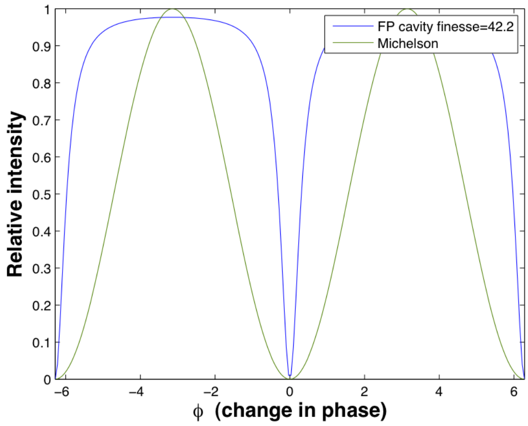

Figure 4.1: The sensitivity of a Michelson interferometer to particle displacement is sinusoidal. A FP cavity of finesse=42.2 is more sensitive to length changes assuming the phase is 'biased' to a sensitive point. For the FP sensor, ϕ assumes essentially the same form as in Eqn. 4.3, where ξ is understood to be cavity length.

not appropriate. The phase for the MI is simply dependent on acoustic particle displacement, the phase for the FP interferometer is dependent on the relative displacements of two nearby mirrors, and so is a more complex, wavelength dependent quantity.

Like the FP sensor, a MI sensor may be made transparent to the excitation laser wavelength by use of dichroic mirrors, which allows a greater flux of light to the tissue, and hence an increased signal. However, standard metal coatings were used in this project due to the relative ease by which they could be manufactured (see Appx. A). This allowed for modifications in design to be rapidly implemented, reasons for which are discussed further in Sec. 5.2.

4.2.1 Quadrature Phase Detection

A standard Michelson interferometer shares the problem with the FP detector that the sensitivity varies depending on the positions of the mirrors as seen in Fig. 4.1. This is an issue, because the same amplitude acoustic wave will cause different changes to the intensity if the position of the mirror is moved even slightly. This issue can be overcome by the use of quadrature phase detection (QPD), which is shown schematically in Fig. 4.2. QPD ensures that whatever the position of the mirror, the sensitivity is always high. Furthermore, it allows unambiguous identification of which direction the mirror has moved. QPD essentially creates two Michelson interferometers in the same device, where the interference phase of one always lags behind the other by $\pi/2$. This is done using two orthogonal polarisations, which act independently from one another, but have a known phase relationship. Light from the probe laser is linearly polarised at an angle of 45° from the 'vertical'. This is equivalent to creating a superposition of two orthogonal polarisations of equal intensity: one vertical, one horizontal. In one of the arms of the interferometer, a $\lambda/8$ wave plate is inserted. This retards the phase of one of the

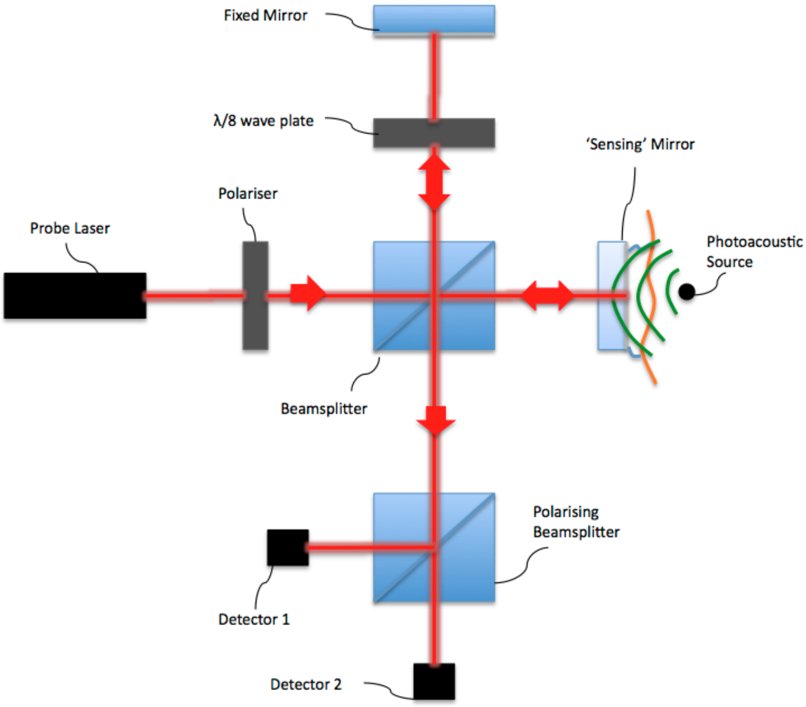

Figure 4.2: A schematic of the Michelson interferometer photoacoustic sensor built in this project. Ultrasound passing through the sensing mirror change the path length of the light slightly, which alters the phase of the interference pattern. The quadrature phase detection allows high sensitivity to be achieved, whatever the mirror positions.

polarisations (the vertical say) by $\pi/2$ ($\pi/4$ in both the forward and return journeys) compared to the other. The beam then recombines with the other beam, where both polarisations have equal phase. This recombined beam is then split at a polarising beamsplitter. The result is that one interference patten (the vertical in this case) lags behind the other by $\pi/2$ in phase.

4.2.2 Sensitivity of the Michelson Interferometer

Given a mirror movement of a certain distance ξ, even a normal Michelson interferometer (suitably calibrated), can determine the distance ξ just by looking at the interference intensity. One advantage of quadrature detection, is that the *direction* of movement can always be determined, which is not always the case for a standard MI. However the main advantage to quadrature detection, is that the *sensitivity* is always high. In this sense, *sensitivity* is the modulation in the intensity per unit change in phase. For a standard MI, this is simply the gradient of Eqn. 4.2, which can vary between 0 rad^{-1} and $I_0/2$ rad^{-1}. For a MI with quadrature detection, the sensitivity varies between between $I_0/2$ rad^{-1} and $I_0/\sqrt{2}$ rad^{-1} as shown in Fig. 4.3. This is simply the sum of the absolute optical modulation sensitivities for two single MIs which are $\pi/2$ out of phase.

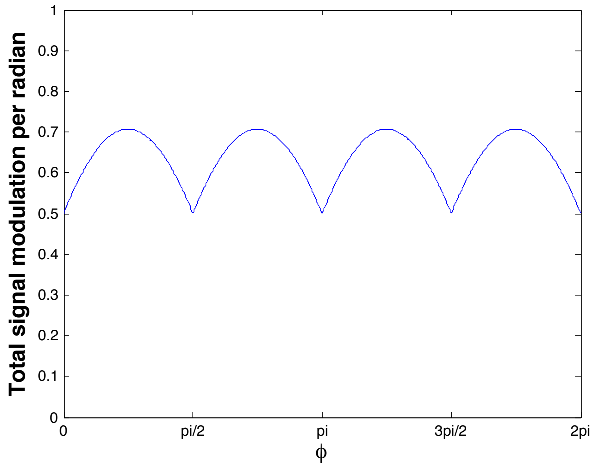

Figure 4.3: The sensitivity of a Michelson interferometer (MI) with quadrature phase detection is always at least as high as a standard MI. This is due to the dual interference detection system it incorporates. Despite its ossification behaviour, the sensitivity is sufficiently uniform to not bother with biasing it to the most sensitive region, as must be done with the Fabry-Perot interferometer.

To recover the change in phase given a certain modulation of the two detector outputs, the following equation is used:

$$\phi = atan2(I_a, I_b) \tag{4.4}$$

where $I_{a,b}$ are the outputs of the two detectors which have been scaled between -1 and 1.

It is of interest to know the sensitivity of the detector in terms of response to applied acoustic waves. In order to do this, Eqn. 4.1, may be used, where optical reflectance R_{opt} is simply replaced with intensity, I:

$$S = \frac{1}{I_0}\frac{dI}{dp}. \tag{4.5}$$

Since the Michelson response is given in terms of particle displacement, the chain rule may be invoked and Eqn. 4.5 becomes:

$$S = \frac{1}{I_0}\frac{dI}{d\phi}\frac{d\phi}{d\xi}\frac{d\xi}{dp}. \tag{4.6}$$

$\frac{dI}{d\phi}$ may be taken to be 0.5, which is the minimum sensitivity shown in Fig. 4.3. $\frac{d\phi}{d\xi}$ may be found simply by differentiation of Eqn. 4.3. To find $\frac{d\xi}{dp}$, Eqn. 2.8 can be differentiated with respect to p_0, and the peak value taken, recognising that this step limits the validity of the sensitivity calculation to sinusoidal signals only (which is not a problem given any signal can be represented as a sum of sinusoids). Also, if it is assumed that the mirror substrate is made of some material other than the propagation medium, then Eqn. 4.6 may be multiplied by the pressure transmission coefficient of Eqn. 2.22. Substituting all this into Eqn. 4.6 yields:

$$S(\nu) = \frac{n}{c\rho\nu\lambda}\frac{2z_2}{z_1 + z_2} \tag{4.7}$$

where λ refers to the probing laser wavelength. Also, $c\rho$ can be replaced with z_2 according to Eqn. 2.20 (since these quantities refer to the material of the substrate). This leads finally to the general expression for the sensitivity of the MI:

$$S(\nu) = \frac{2n}{\nu\lambda(z_1 + z_2)}. \tag{4.8}$$

The material eventually used for the construction of the mirror substrate was glass (see Chap. 5.2), and it may be assumed that the propagation medium is water. Substituting some suitable numbers into Eqn. 4.8, gives the frequency dependent proportional signal modulation per pascal of acoustic pressure, which is more intuitively expressed as a percentage:

$$S(\nu) = \frac{22}{\nu}\ \%\mathrm{HzPa}^{-1}. \tag{4.9}$$

For a typical frequency PA wave of 1 MHz, and converting the unit of pressure into bar, a direct comparison of sensitivity between the Michelson interferometer and the reflection based detector can be made. Under these circumstance, the Michelson sensor has a sensitivity of 2.2% grey level modulation per bar. This compares with the 0.19 to 0.81% of the optical reflectance detector. However the modulation level of the Michelson detector decreases as $1/\nu$, which means that at frequencies greater than about 5 MHz, the reflection based detector becomes more sensitive.

It is worth now having a short discussion about the particle displacement at the boundary of two adjoining media. In the above equation, it was assumed that the displacement at the boundary of the propagation medium and the substrate (which is where the mirror surface is), is the same as the displacement within the substrate. This is sensible, since the motion of the particles in the substrate can only have been influenced by the forward propagating wave, which for all practical purposes, originated at the interface. The particle displacement after any number of interfaces can simply be found by recursive application of the pressure transmission coefficient to the pressure, then application of Eqn. 2.7.

As will be shown in Sec. 5.2, one configuration of the sensing mirror was to have the mirror surface on the far side of the substrate from the propagation medium, facing air. Since the acoustic impedance of air is orders of magnitude smaller than most solids and liquids, it may be considered a free boundary. A short analysis reveals that under these circumstances, the displacement of the free boundary is twice that of the particle displacement within the substrate (where the acoustic impedance of air is set to zero in the very last step):

$$\xi_{free} = 2\xi_{internal}. \tag{4.10}$$

This appeals to intuition, because at the free boundary the same pressure need only stretch the substrate, rather than stretch one section, while compressing another. Thus, if the mirrored surface is on a free boundary, the sensitivity of the Michelson sensor would be doubled.

It is also possible that the use of multiple detectors for quadrature detection could help to filter out noise form the detectors themselves. There would be no correlation between the noise in the different detectors, and so may provide a method of filtering which could reduce noise level.

4.2.3 Ideal Optical Detectors for the MI

Like the 2D optical reflectance based detector, the Michelson interferometer is capable of measuring the pressure distribution over its entire 2D surface without the need for any biasing. This is because QPD gives the MI approximately uniform sensitivity for all ϕ. This is a significant advantage in terms of data acquisition speed, because it removes the need to raster scan, as must be done with the Fabry-Perot interferometer.

To take the pressure measurements (or displacement measurement in this case) the optical intensity modulation of the entire interference pattern must be measured at very high speeds. Ultra-fast-framing CCD cameras can capture images at rates of hundreds of megahertz, but can typically only take up to 20 images at a time[50]. Time is then required (at least 500 ns) to 'dump' the image data into memory before another set of ultra-fast images can be taken. For this reason, many cycles may have to be performed with a CCD, with images being captured at slightly different times each cycle. Ultra-fast-framing CCDs have been created which can capture more than a hundred consecutive images, however 'dump' time is increased to 20 ms[51].

4.3 Experimental setup

The experimental apparatus actually used in the project is shown in detail in Fig. 4.5.

A pair of lenses were added before the initial polariser, which expanded the HeNe interrogation beam to 1cm diameter. This allowed illumination of a large surface of the sensing mirror, so any part of it could be 'interrogated' without moving the laser.

Acquisition time is only an issue when conducting experiments *in vivo*. Given that all imaging work was conducted with phantoms in this project, it was unnecessary to use high speed (high cost) fast-framing CCDs. Instead, high speed photodiodes were employed, and their positions raster scanned to form images.

An aperture was placed in front of the polarising beamsplitter, and the assembly, including the photodiodes, was mounted on an (x,y) translation stage. This arrangement allowed measurements to be taken in a raster like fashion, across the surface of the sensing mirror.

A piezoelectric stack was placed in the mirror mount of the 'fixed' mirror. This allowed electronically controlled movement of the mirror so the fringe pattern could be cycled though

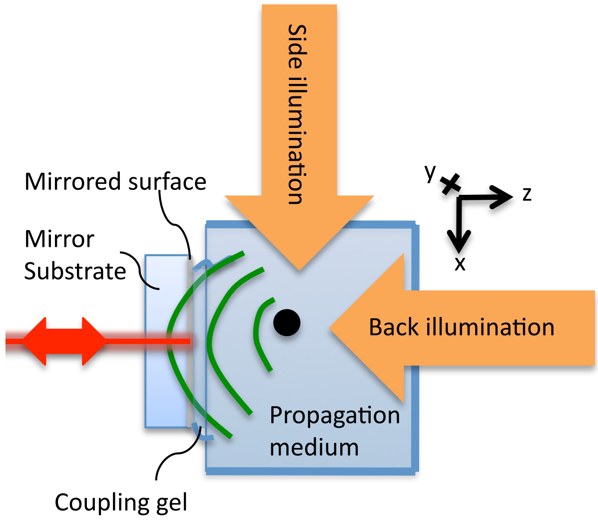

Figure 4.4: A diagram of the basic setup of the absorber and sensing mirror used in this experiment.

on demand. This was required for calibration of intensity modulation depth.

A slight alteration to the proposed design shown in Fig. 4.2 required the use of a variable retarder instead of a $\lambda/8$ waveplate. This was necessary to adjust for any birefringence native to either the beamsplitter or the sensing mirror. Birefringence in either would mean that a 'rigid' $\lambda/8$ retarder would cause the the difference in phase between the two polarisations to vary from $\pi/2$. The variable retarder however, allowed adjustment so that the desired $\pi/2$ phase difference could be achieved irrespective of the birefringence in other components of the device.

The photoacoustic source was placed in a glass walled cell, which was open at the top. This allowed illumination by the excitation laser to occur through either the 'side' or the 'back'. 'Side mode' illumination was the predominant method used, as it allowed easy lateral translation of the phantom without the need to adjust the direction of the illuminating laser (see Fig. 4.4). This also removed the need to use a dichroic mirror, making the prototype simpler to modify.

The wall of the cell facing the mirror was made of a thin (< 10 μm) polymer film, which stopped the sound propagation medium (water or Intralipid) from leaking out. Polymers are acoustically well matched to water, so the film was considered acoustically transparent. The film was then coupled to the sensing mirror with a thin layer of water-based ultrasound coupling gel. This can be seen schematically in Fig. 4.4.

The photoacoustic source, or 'absorber' (generally a thin, ink-filled tube), could be held in place by a clamp which was attached to a translation stage. This allowed the position of the absorber to be precisely adjusted. In addition, the entire sensing mirror/cell/absorber assembly could be placed on a translation stage. This was necessary when the aperture in front of the detectors was made very small and the beam expanders were removed to increase beam intensity. By moving the whole assembly, a scan could be performed without the need to adjust beam or

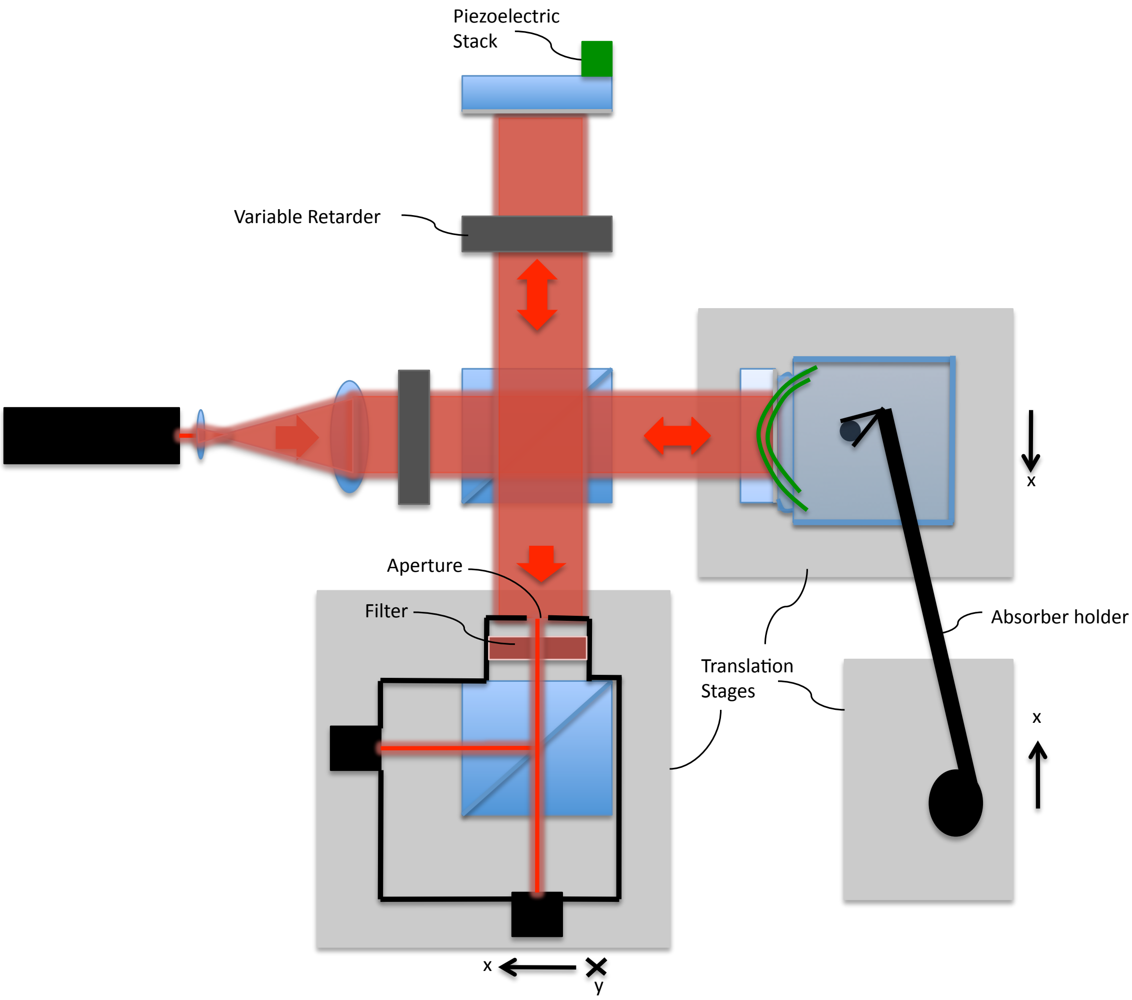

Figure 4.5: A diagram of the actual experimental setup of the MI sensor.

detector position.

Chapter 5

System Development

Despite the effort invested in the design phase of the MI detection system, there were several modifications made during experiment. The need for some of these modifications, which were centred around changes to the sensing mirror, only became apparent after all other components of the system had been implemented. This chapter will focus on the factors that led to the evolution of the system, and the convergence on a final design.

5.1 Signal Analysis

The process of obtaining a pressure measurement from the Michelson Interferometer detector was somewhat less direct than simply measuring the output of the photodiodes. This section outlines the methods involved in signal analysis: from measurement of photodiode output, to the preparation of data for input into the reconstruction algorithm. A flow chart of the process can be seen in Fig. 5.1.

The first phase of analysis involved taking the output voltage of the photodiodes, and scaling them into the range of a sine wave, so that the change in phase due to the mirror displacement could be calculated. Photodiode output was recorded on high sampling rate 8-bit digital oscilloscopes. Firstly, the maximum and minimum voltage outputs needed to be measured, for a full interference fringe modulation. This was done by moving one of the interferometer mirrors through a distance (using a piezoelectric stack), so that the fringes moved through at least one cycle. The output of both photodiodes were recorded, so each channel could be scaled independently. This 'calibration' step was necessary every time a new point on the sensing mirror was interrogated, since slight non-uniformities in the mirror lead to variable fringe size. This in turn leads to variable modulation depth, and hence varied minimum and maximum output voltages of the photodiodes.

Once a calibration had been done, photoacoustic measurements could be taken. This required the use of four oscilloscope channels, two for each photodiode. One of the channels from each

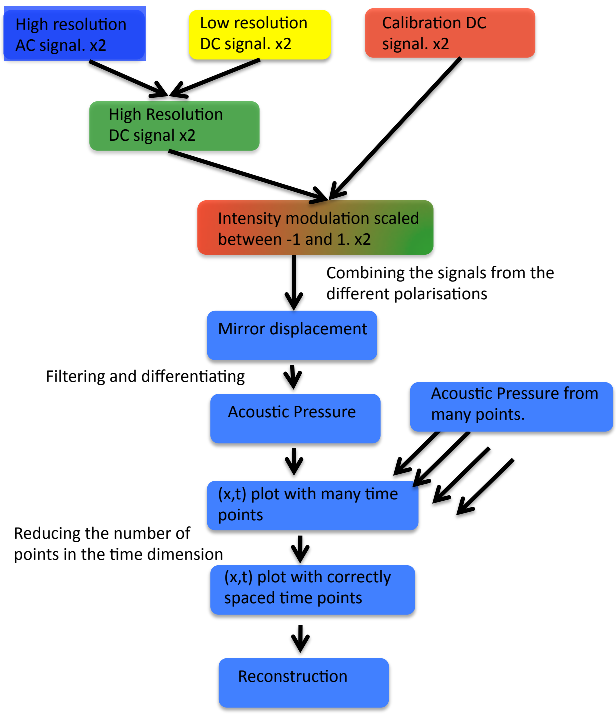

Figure 5.1: A flow chart of the processes involved in converting photodiode output into a tomographic reconstruction of the initial pressure distribution.

photodiodes was DC coupled, and the voltage scale was set to allow the minimum and maximum voltage in the one screen. This was necessary, because signals were averaged over several seconds, so the DC output voltage could vary significantly. Unfortunately at such a large voltage scale, the desired PA signal could barely be seen. For this reason, one channel from each photodiode was also AC coupled, and the voltage scale set very low, so very small signals could be seen. If the data recorder had a higher bit depth, this would not be necessary, and the AC and DC coupling could be replaced by a single high detail DC channel.

The calibration, AC, and DC results were then combined in the following manner: The average DC voltage for each channel was added to the corresponding AC channel. Then the resulting voltage signal was scaled by the calibration, so that the maximum voltage of the calibration corresponded to 1, and the minimum corresponded to -1.

The two scaled results were then put into Eqn. 4.4 to find the change in phase, and this was converted to mirror displacement using Eqn. 4.3.

The displacement signal was usually noisy, which presented a problem given that the derivative needed to be taken to find the pressure. A lowpass digital filter was therefore applied to the displacement before the derivative was taken. The cut-off frequency for the filter was found through a process of trial and error, and was taken to be about $3MHz$. If smaller, more complex phantoms were imaged, it would be necessary to increase this cut-off frequency, which would result in a more noisy derivative signal.

As mentioned, the pressure was found according to Eqn. 2.5, by numerical differentiation of the filtered displacement signal.

To feed the data into the reconstruction algorithm, the pressure signal from a set of x, y points had to be combined into a single array. In reality, only horizontally symmetric objects were imaged, so only a one dimensional scan in the x direction was required. The high sampling frequency of the oscilloscope meant that there were many more points in the time dimension than in the x dimension. To satisfy requirements of the reconstruction algorithm, time points were evenly sampled from this array at intervals of $\Delta t = c\Delta x$.

The whole analysis was automated, and took several minutes to run on a standard desktop computer. However the majority of this time was spent filtering the signal, which could be parallelised to significantly reduce computation time.

5.1.1 Signal Amplification

The small mirror displacement created by a PA wave resulted in a typical signal modulation of the order of 1%. The optical detection system consisted of a pair of photodiodes connected to a digital oscilloscope. It was therefore not optical modulation that was directly recorded, but rather photodiode output voltage. It was desirable that photodiode voltage output be large, because the oscilloscope could only register voltages to a depth of 8 bit, and the smallest voltage division was 2 mV. If the signal produced from the photodiodes was only a small fraction of 2 mV, then the low bit depth became apparent as the recorded signal would take on step like features. The simplest way to increase the output voltage was to increase the aperture size in front of the photodiodes. This was undesirable however, because the aperture size determined the resolution at which scans could be performed.

The other significant constraint of the optical detection system was the high speed response required. Unamplified photodiodes were unsuitable for both these reasons. A sufficently high voltage signal could be obtained if the photdiode were coupled to the ossciliscope with a 1 MΩ resistor, however the long rise and fall times completely destroyed the shape of the signal. Conversely, a high speed response could be achieved using a 50 Ω coupling, but this resulted in an unacceptably low voltage.

The solution was to use amplified photodiodes. The amplification stage increased the voltage so the bit depth of the oscilloscope was not an issue. and removed the capacitative effect of the photodiode, so a fast response could be achieved.

In fact, the initial amplified photodiodes purchased from Thorlabs had insufficient bandwidth at the required amplifications, so they were eventually replaced by a custom amplifier built into the original unamplified photodiodes. This resulted in a voltage modulation which was sufficiently large even when the aperture diameter was reduced to slightly less than 1 mm.

The factor limiting the reduction in aperture size further was not the bit depth of the oscilloscope, but rather the noise from the photodiodes due to the amplification stage. For most of the images shown in the Chap. 6, an aperture size of slightly less than 1 mm was small enough to resolve the configuration of the absorber. To test the limits of resolution however, it was desirable to decrease the aperture size still further, to around 200 μm.

The noise in the signal was almost entirely from the photodiodes, with little or no noticeable contribution from the laser itself (at least on the time scales which were of any consequence). To increase the modulation in output voltage, while keeping the noise at the same level, the laser power was simply increased. In practice this was done by removing the beam expander, so that only one point on the sensing mirror could be interrogated. This was not a significant disadvantage, since it was usually the absorber which was moved rather than the detector, which speed up data collection as previously mentioned.

Using the unexpanded beam, the aperture could be closed to its smallest diameter ($\approx$ 200 μm), whilst the output voltage modulation of the amplifier was at its absolute maximum (which was about 8 V). In fact, the aperture size could have been halved whilst still keeping this maximum modulation, since the beam had to be attenuated to avoid saturating the amplifier when using the 200 μm aperture.

Further development of the Michelson sensor would entail the use of CCDs rather than photodiodes. The methods of signal analysis and amplification needed in this configuration would differ significantly from those used here, though many of the considerations would be the same.

5.2 Internal Acoustic Reflections and Rayleigh Waves in Sensing Mirrors

One of the most important components of this project was the development of the 'sensing mirror' to be used in the interferometer. The initial design was based around trying to maximise particle displacement through suitable choice of material, however factors revealed through experimentation relegated impedance matching a minor consideration.

5.2.1 Internal Reflections

The first photoacoustic measurements taken were of a simple cylindrical absorber so that they could be compared with the simulation in Fig. 3.2. All the results in Fig. 5.2 were taken with the absorber directly in front of the mirror region being interrogated. These results are for qualitative comparison only, as quantities such as laser power, and exact depth, varied from test to test. In addition, some of the earlier tests were performed before the system was set up to take calibrated measurements, which is why the displacements have been normalised to unity. It should also be noted that in all the figures, the signal around $t = 0$ is not a photoacoustic wave passing through the mirror, but a combination of excitation laser registered by the photodiodes, and noise generated by the trigger signal.

The first mirror used was 2 mm thick aluminised PMMA. It was initially hoped that the acoustic wave would pass through the mirrored surface, and then rapidly be absorbed, since polymers are good acoustic absorbers. A quick comparison between the simulated displacement in Fig. 3.2, and the measured displacement for this mirror (Fig. 5.2a), shows that this was not the case. On close inspection, it can be seen that there is an initial rise at around 3 μs, then another rise just after the first rise had peaked. The initial rise was interpreted as the desired signal of the displacement wave passing through the mirror surface. The second rise, about 1 μs after this was almost certainly due to the same displacement wave, after it had reflected off the front surface of the mirror. The continued oscillations were thought to be caused by repeated reflections, off both the front and rear surfaces. The apparent decrease in amplitude was likely due to some of the wave coupling back into the propagation medium with each reflection off the back surface.

Glass was undesirable as a mirror substrate due to its large acoustic mismatch with water, however due to the availability of standard optical quality glass mirrors, these were also tested for use as a sensing mirror. A typical response from a 5 mm thick glass mirror is shown in Fig. 5.2b. It can be seen that the signal is different to that of the 2 mm plastic mirror, however there are still very large reflections as expected. A 9.5 mm thick glass optics mirror was also tested, however the results were qualitatively similar. It should be remembered that some of the measurements were not made using the final calibrated setup, so quantitative comparisons between the signal strength and noise are not appropriate.

The simplest way to remove the reflections, was to remove any boundaries from which the wave could reflect. In practise, this was done by making the mirror thickness so large that by the time the wave reached the front surface, enough time had passed that any further signal was of no interest. The reconstruction algorithm only requires $t_{\max} = \frac{x_{\max}}{2c}$, where $x_{\max}$ is the total lateral scan distance, so any further signal could be ignored. The results of using thicker mirrors can be seen for PMMA and glass in Figs. 5.2c & 5.2d respectively. In this case, a single clear pulse is present, similar in form to the simulation.

One glaring difference is the negative displacement after the initial positive pulse. The reasons behind this were never fully explained, though there are a number of possibilities. It is possibly due to the pressure pulse being more complicated than that simulated. This is plausible considering the fact that the absorbing ink was inside a silicone tube, whose acoustic properties were unknown. It is also possible that the negative displacement is due to the mirror recoiling back with under damped oscillation. Possibly a more realistic explanation is that the negative displacement is a consequence of Rayleigh waves being generated at the surface, which will be discussed in greater detail in the next section.

The absence of clear reflections in the 20 mm glass mirror was due not only to its thickness in the propagation direction, but also its large lateral extent. This allowed the incident wave to

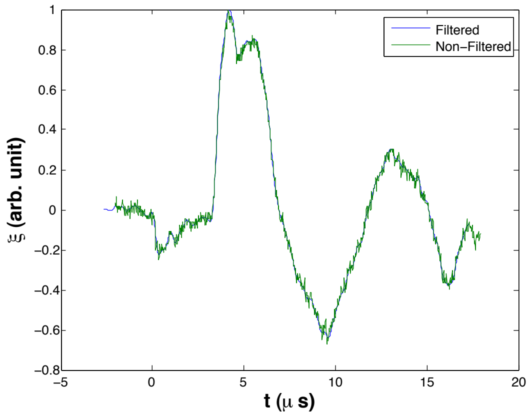

(a) $2mm$ PMMA miror.

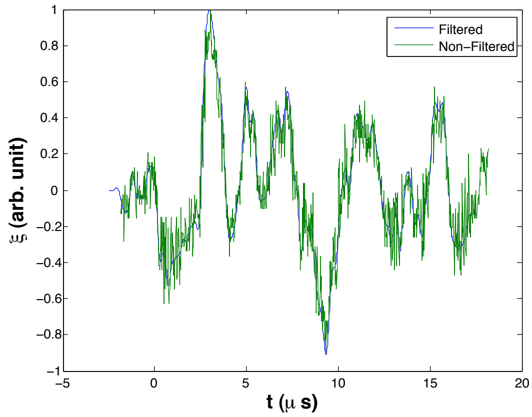

(b) $5mm$ glass mirror.

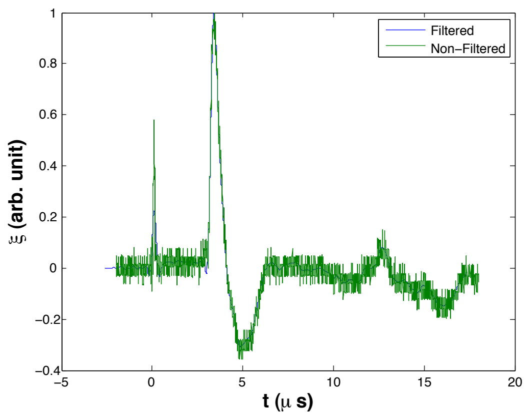

(c) $25mm$ PMMA mirror.

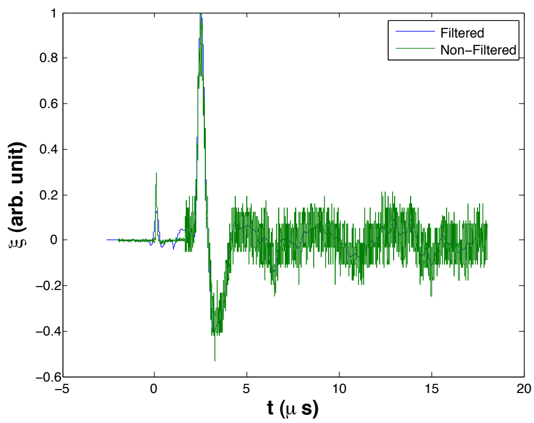

(d) $20mm$ glass mirror.

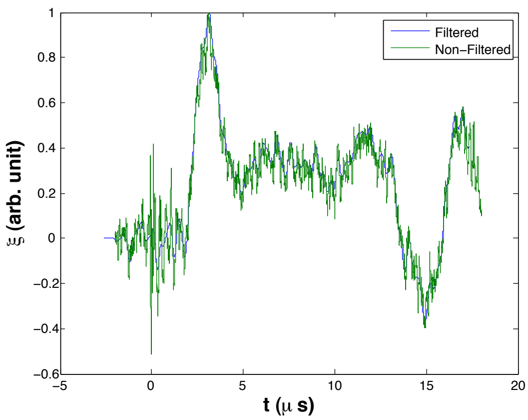

(e) $1mm$ glass mirror.

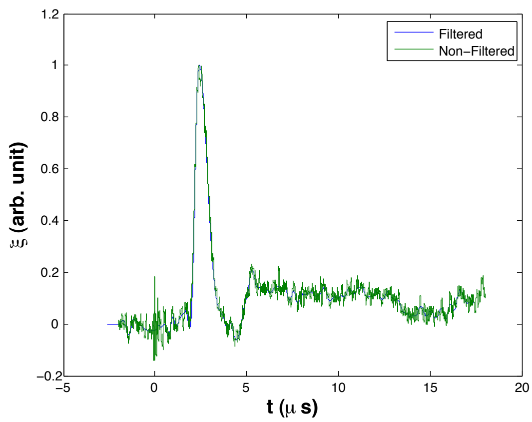

(f) $0.15mm$ glass mirror.

Figure 5.2: Mirror displacement for a variety of mirrors, some of which show internal reflections.

spread out significantly, so that by the time it had reached the mirror surface again, its intensity had been significantly reduced. In plastic however, the long distance of propagation removed the reflections, since the speed of sound in polymers is typically less than half that of glass. Thick polymer mirrors are not made by standard optics manufacturers, so these were polished and coated on site by the author (details are available in Appx. A).

Another way to remove internal reflections was to make the mirror substrate so thin that it was acoustically equivalent to a zero thickness plane. For this to occur, the substrate width must be appropriately smaller than the acoustic wavelength. For glass, at a frequency of 1 MHz, the acoustic wavelength is around 5 mm. It can be seen in Fig. 5.2e, that reducing the substrate width to 1 mm does improve the signal compared to slightly larger substrates, but is far from eliminating interference altogether. Reducing the substrate width further to 150 μm returned the signal to the expected single peak. It can also be seen that the trailing negative displacement in this case was less pronounced than for the thick substrates. It is also worth noting that the mirror coating was on the 'front' side of the substrate in this example. This was simply to protect the mirror surface, and reversing the orientation had no significant effect on signal. Again, these non standard substrates were coated on site, which allowed for rapid implementation.

A possible disadvantage to removing internal reflections by reducing substrate width, is that the sensor will only function properly when looking at sufficiently low frequencies. The effect higher frequencies had on the 150 μm mirror could not be explored because no method of reliably generating frequencies greater than 1 MHz was available. If higher frequencies do pose a problem, the substrate thickness could relatively easily be reduced to 30 μm using commercially available optics, however further reduction in thickness may be difficult.

5.2.2 Rayleigh Waves

All the signals discussed in the last section were detected where the source was positioned directly behind the mirror position being interrogated. Under this condition, both very wide, and very thin substrates produce suitably 'clean' signals. However, the first 'lateral scans' revealed a new problem. The term *lateral scan* refers to a set of measurements taken at regular intervals in the 'x' direction (the direction along the mirror plane which was perpendicular to the direction of the cylindrical absorber).

It is worth mentioning that in all the lateral scans shown in Fig. 5.3, it was actually the absorber that was moved, while the position of mirror interrogation was kept constant. This was done simply as a way to speed up data acquisition, since only one calibration had to be made (see Sec. 5.1). In most circumstances this made no difference to the detected signal, because only relative position was important. The possible exception to this was when the absorber was moved very close to the edge of the glass cell. Under these conditions, multiple acoustic reflections off the cell and silicone tube may have interfered with the signal, though no such complications can be seen in any of the graphs in Fig. 5.3.

Using the very thick substrates it was found that at increasing lateral distances from the absorber the single displacement pulse began to split into two pulses, one lagging behind the other. This became very clear on inspection of graphs such as those in Fig. 5.3 where the pressure is shown in the (x, t) plane. In creating such plots, the absorber was placed at approximately $x = 1$ mm, around 2 mm from the surface of the mirror. In all the plots shown, the pressure is a single clean pulse when measured directly in front of the absorber (except for the 1 mm substrate, which was shown in last section to produce results of borderline quality). However, in all the thick substrates, this initial wavefront can be seen to split into two at larger distances from the source. This behaviour was determined to be a result of Rayleigh waves propagating on the surface of the mirror.

Rayleigh waves are a deformation which propagate along the surface of an elastic material, where the amplitude of the wave decreases exponentially with depth. They have particle displacement both parallel and perpendicular to the surface. Rayleigh wave velocity c_R, is a complicated parameter to compute. It is usually given as a proportion of shear wave velocity c_s, as a function of the Poisson's ratio of the medium. For any real medium, Rayleigh wave velocity can vary from 0.87 c_s to 0.96 c_s[52]. An in-depth discussion of Rayleigh waves is available in Ref. [52]. Technically, when the surface of the elastic medium is in contact with a liquid, the surface waves are referred to as *leaky* Rayleigh waves, as the energy is radiated back into the liquid as the surface wave propagates.

It was proposed that Rayleigh waves had been induced in the mirror substrate when the photoacoustic wave first reached the surface. From this point on, the mirror displacement at any point on the surface of the mirror was due to a superposition of the incoming PA wave and the perpendicular component of the Rayleigh wave.

Using values for sheer wave velocity and Poisson ratio in PMMA[53], and a conversion plot in Ref. [39], Rayleigh wave velocity in PMMA was calculated to be $c_R = 1300\ \mathrm{ms}^{-1}$, which is slightly lower than the speed of sound in water. Likewise, for glass, c_R was found to be around $c_R = 3000\ \mathrm{ms}^{-1}$, which is approximately double the speed of sound in water.

Understanding the variability in Rayleigh wave speed helps to interpret the results in Fig. 5.3. For instance, a comparison between the lateral scans for different substrates, reveals that the initial wavefront seems to 'split' into the Rayleigh component and standard component at different rates. It was expected that for plastics, where the Rayleigh wave is slower than the longitudinal wave in water, that the longitudinal wave would arrive earlier at large distances from the source, and vice versa for glass. While some of the plots *could* be interpreted in this manner, it is far from conclusive. In fact, objectively, it appears as though the Rayleigh wave leads the longitudinal wave in every case. The reason for this not properly understood. It is known that interactions with the liquid increase the speed of Rayleigh waves, and that the increase is more pronounced for lower-density solid media. However it was thought that this effect would only be slight.

There is always the possibility that the observed splitting is not due to surface waves, but

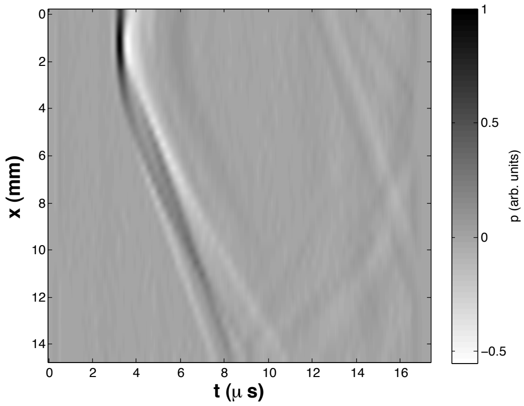

(a) 25 mm PMMA miror.

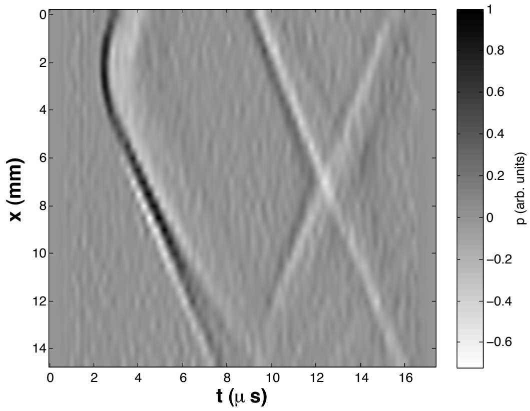

(b) 25 mm polystyrene mirror.

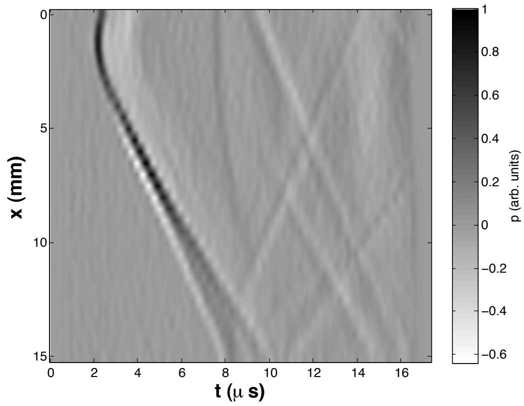

(c) 7 mm polycarbonate mirror.

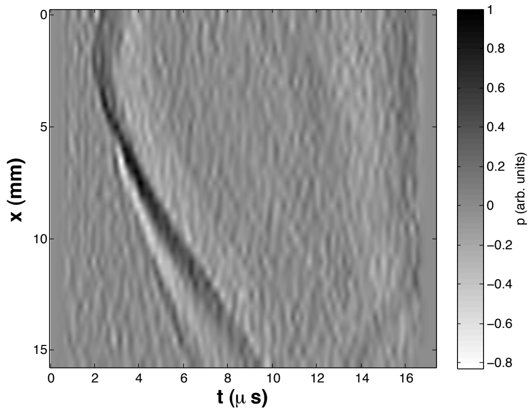

(d) 1 mm glass mirror.

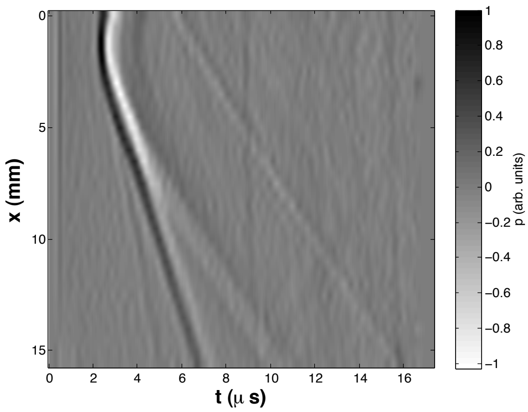

(e) 20 mm glass mirror.

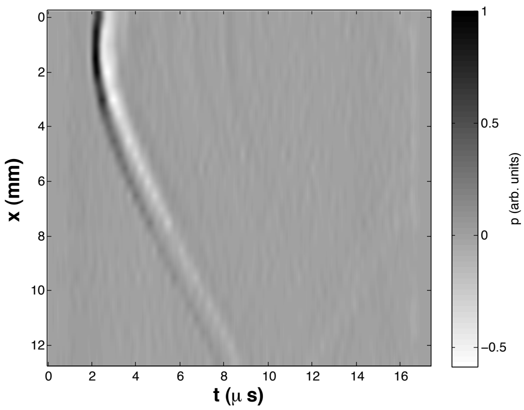

(f) 0.15 mm glass mirror.

Figure 5.3: The above graphs show the pressure detected at the sensing mirror for a set of points along the x axis. The source was a single cylindrical ink absorber oriented perpendicular to the x and z axes.

some other phenomena. However this seems unlikely, especially when Fig. 5.3f is considered. This plot is striking in that is shows no evidence of the splitting observed in all other substrates. This is an expected if surface waves are the cause of the splitting, because the 150 μm substrate is simply too thin to sustain them. The penetration depth of Rayleigh waves are on the order their wavelength. If it is roughly assumed that the frequency of the Rayleigh wave is equal to the frequency of the initial acoustic wave, this would give a penetration depth in glass of ≈ 3 mm. This is possibly small enough to propagate in the 1 mm substrate, but is much to large for the 150 μm substrate.

Pressure lines can be seen in each of the graphs in Fig. 5.3, which are clearly not part of the initial wavefront. These simply correspond to acoustic reflections off the side of the cell which contains the propagation medium. For the case of the larger substrates, some of these lines may also be reflections of the surface wave off the boundary of the mirror. In either case, they pose no concern regarding signal quality, because they can be removed by creating a suitably large cell and mirror.

In summary, it was found that the only mirror which eliminated both internal reflections and Rayleigh waves was the 150 μm thick one. Indeed, though this mirror was presented alongside the others, it was actually introduced as a solution to the problem of Rayleigh waves. The use of polystyrene and polycarbonate as substrates were also initially proposed as a solution, as their properties make Rayleigh waves more 'leaky'. It was reasoned that a very leaky mirror would radiate away any Rayleigh waves before they had a chance to interfere with the true signal, however as can be seen, this approach was unsuccessful.

While the 150 μm mirror produced a signal of sufficient quality to act as a PA sensor, mounting it to be interferometrically stable was problematic. This was eventually solved by bonding it around the edge to a larger substrate, as will be seen in the next section.

5.2.3 Signal from the Excitation Laser

While the very thin (150 μm) mirror solved the problems of internal reflections and Rayeligh waves, it did produce some non ideal signals. The mirror from which the following data was taken was the coated 150 μm substrate, which had been bonded to an optical glass flat.

Fig. 5.4a shows a small PA pulse from a hair, with peak at around 2 μs, on top of a large anomalous peak of lower frequency. Fig. 5.4b shows the same anomalous peak, but on a slightly longer time scale, and with no absorber. Initially it was thought that this was a PA signal from some absorption by the water. To test this, the water filled cell was removed and the excitation laser aimed directly at the mirror. The result can be seen in Fig. 5.5.

It can be seen on the short time scale plot, that even without the cell attached to the mirror, the anomalous signal persists. This suggests that the unwanted signal is not a PA wave from the water, but is a result of direct interactions between the excitation light and the mirror. While no firm conclusions have yet been drawn, there have been some well backed-up hypotheses.

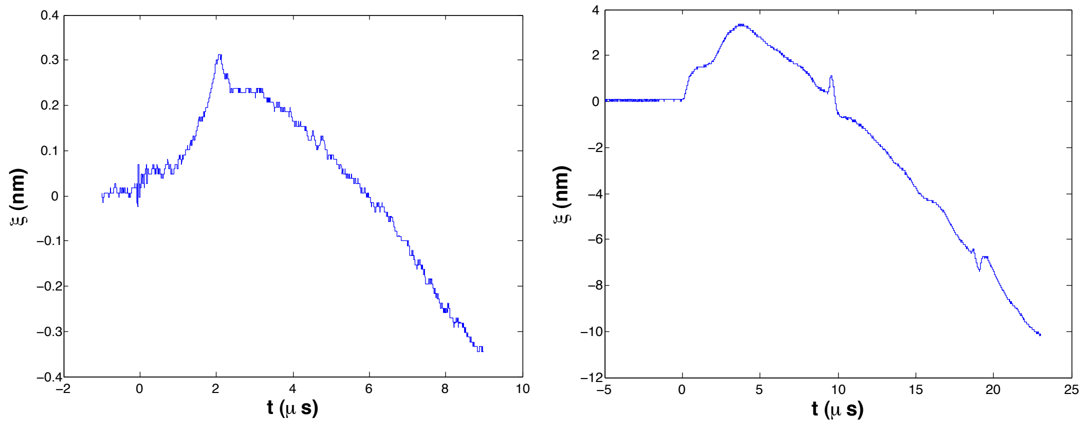

(a) With absorber.

(b) Without absorber.

Figure 5.4: Mirror displacement using the 150 μm thick mirror. The signal from the absorber can be seen in a), however it is less noticeable because of the anomalous signal that exists even without an absorber. b) shows that this anomalous signal is stronger when the excitation laser is directed toward mirror, rather than parallel to it. The graphs show the presence of Rayleigh waves in all but the 150 μm thick mirror.

Firstly, the signal must be considered in two parts: the initial positive displacement, which lasts on the order of 5 μs, and the large negative displacement, which has a duration around 1000 times longer. Looking at Fig. 5.5a, it can be seen that the rise begins immediately after the laser pulse (at $t = 0$). Furthermore, it is apparently moving at its fastest speed directly after the laser pulse. This rapid impulse suggests that photon recoil from the excitation laser may be the source, since it would deliver all its momentum in the first 100 ns (the excitation laser pulse length at low powers).

The most interesting feature of the large, slow, negative component is that it *is* negative. This corresponds to the mirror moving in the direction of the excitation source. It is difficult to imagine how the mirror could have been *pulled* in this direction, so a more plausible explanation is that it was *pushed* from the opposite side. It is suggested that this is a result of thermal expansion of the air between the mirror and the optical flat. When the excitation laser hits the mirror, some fraction of it will be absorbed by the (less than perfect) gold coating. This heat is then slowly transferred to the air gap, there the corresponding thermal expansion leads to the mirror being pushed in the negative direction. Relaxation to the resting position would occur as the air cools, and contracts. This is supported by the time scale of the relaxation of Fig. 5.4b.

One criticism of the photon recoil explanation may be the qualitative difference of the initial rise depending on whether the water filled cell is present or not. When the cell is present with an absorber, the rise does not seem as linear, which is also true when the cell is present without the absorber. It is possible then, that a PA signal *is* generated by the water, and that it coincidently has a similar form to the displacement formed by photon recoil. It should also be asked why

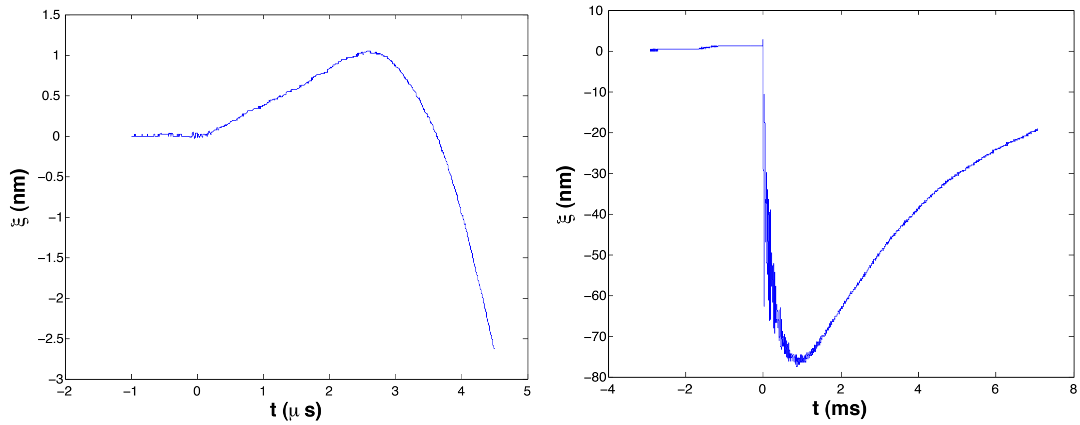

(a) Short time scale.

(b) Long time scale.

Figure 5.5: The unwanted signal from the thin mirror persists even when the water filled cell is removed. a) shows the initial rise probably due to photon recoil. b) possibly shows the slow expansion and contraction of the gas in the air gap between the mirror and the optical flat.

no such rise was seen with other mirrors on thicker substrates. No satisfying answer can yet be given to this and other questions, and further experiments are needed to confirm what processes are actually occurring.

5.3 Final Mirror Design

As was discussed in the last section, it was eventually found that the only suitable mirror for detecting PA waves was the coated 150 μm substrate. This was created by coating a glass microscope coverslip with a thin layer of gold. More problematic was mounting this very thin mirror so that it was stable enough to take measurements. The first attempts were focused around simply taping the coverslip to a mirror mount and adjusting the angle to find the fringes *after* the mirror had been coupled to the propagation cell. This did work to some extent, however the fringe pattern was only stable for a matter of minutes before it shifted significantly. This was clearly unacceptable to the purposes of image formation, and offered no hope of extension to clinical imaging.

To stabilise the mirror, it was placed on a thick optical flat, and bonded with epoxy around the perimeter. The mirror surface was face down (toward the optical flat), to protect it from damage. The result was a surprisingly stable ultra thin mirror, with a small air gap between the mirror surface and the substrate. The air gap was formed due to a slight capillary action on the unset glue, which was pulled between the flat and mirror around the edge. It was estimated to be on the order of 10 μm thick. This was desirable, since if the mirror was in contact with the optical flat, then there would be the problems of internal acoustic reflections. As it happened, the air gap formed an acoustic insulator, while the glue held the mirror rigidly in place. This

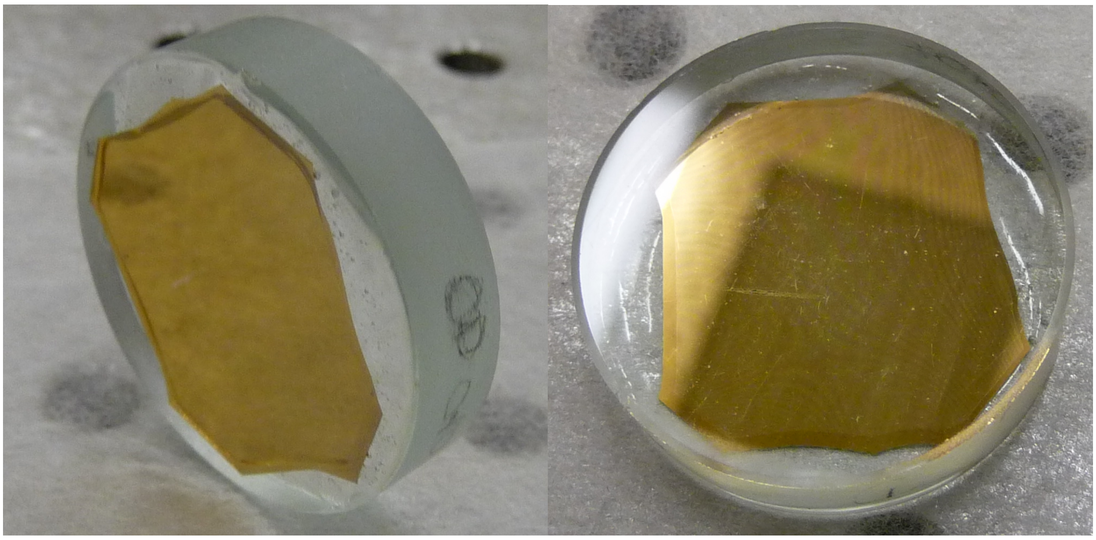

(a) Acoustically coupled side. **(b)** Interferometer interrogation side.

Figure 5.6: The front and back sides of the final sensing mirror are shown. Looking at the interrogation side, a small amount of glue can be seen between the edge of the mirror and the optical flat. The unwanted etalon fringes can also faintly be seen in this image.

mirror can be seen in Fig. 5.6.

If any significant force was applied to the mirror when it was part of the interferometer, the fringe pattern could be seen to distort significantly. However on removal of the force, the fringe pattern would rapidly return to its original configuration. The slight pressure applied when connecting the cell to the mirror with coupling gel had little effect, perhaps momentarily moving the fringes through a single cycle. It can be seen in Fig. 5.6b, that reflections between the mirror and the surface of the optical flat are forming a Fabry-Perot cavity. The weak Fabry-Perot fringes did not significantly alter the intensity of the Michelson interference pattern, but the effect would result in some uncertainty about mirror displacement. This effect could be eliminated if an optical flat had been used which was anti-reflection coated for the interrogation wavelength.

Chapter 6

Photoacoustic Images

The main goal of this project was to develop a photoacoustic imaging system, with a detector based on a Michelson interferometer. The images displayed in this section signify that this goal has been successfully achieved. It also shows, that the prototype system has some limitations, particularly in terms of resolution. Some of these limitations may be relatively easy to overcome with future modifications to the system.

All images taken were two dimensional, even though the system is fully capable of producing 3D reconstructions. As mentioned, this was simply due to the large increase in acquisition time when performing a 2D raster scan with the photodiodes, as opposed to a 1D line scan. All absorbing targets were therefore made (approximately) horizontally symmetric, so a line scan was sufficient to specify the cross section of the original absorption distribution.

For the purposes of testing the imaging system as a whole, laser fluence and, the absorption coefficient of the phantom were set at the upper end of what could be expected in clinical use. Also, the propagation medium was water instead of a scattering medium, because the scattering medium increased the unwanted signal discussed in Sec. 5.2.3. This happened because when functioning in side mode, the only light to hit the mirror was scattered light from the absorber of the surrounding medium.

So while the images shown here have not been produced to be an exact simulation of real living tissue, the setup is not grossly unrealistic.

A Single Ink Absorber

The first image shown is one of the simplest possible configuration: a single ink filled tube in approximately the centre of the field of vision. The silicone tube had an inner diameter of 0.5 mm, and a wall thickness of 0.4 mm.

A comparison between simulation and experiment is given in Fig. 6.1, showing relatively good agreement. The actual reconstruction is more spread out than the simulated one, but both share the arc shaped image artefact. The smaller arc in the lower left hand corner of Fig. 6.1d, was a result of the detection process. As the absorber position was moved rather than the interrogation beam, it is believed that it was moved too close to the edge of the sensing mirror. This may have resulted in multiple reflections from the absorber, or even Rayleigh waves in the optical flat.

Multiple Ink Absorbers

To determine if the system could reconstruct the geometry of slightly more complex phantoms, two ink absorbers were imaged together. The result can be seen in Fig. 6.2. The step size and aperture diameter was larger than for the single absorber above, leading to lower resolution. On inspection of the detected pressure, small acoustic reflections from the silicone tubes could be seen, though these are less obvious in Fig. 6.2a, due to the reduced sampling of points in the time dimension to enable reconstruction.

A scan was also done for four ink absorbers, using a smaller aperture, and step size was used. This shows a less faithful reconstruction, possibly due to the acoustic reflections off the silicone tube. Fig. 6.2d shows a region at $x > 17$ mm where the pressure has been artificially set to zero. This was initially done because the absorber had contacted the side of the cell at this position, however it was realised that zero padding in the spatial dimension could allow more temporal points to be used, and so increase resolution in some circumstances.

Hair Absorbers

To see how high the resolution could be made, the ink absorbers were replaced with human hair (≈ 70 μm diameter). Initially the signal produced was too small for reasonable imaging to be performed, even when the photodetectors and laser were put in the most sensitive configuration. It was reasoned that the hair (which was fine and blond) may have been a poor absorber at 1064 nm, so it was coated with pure undiluted ink and allowed to dry. The resulting signal was large enough to use for imaging, though any sense of realism of the phantom had been removed.

The resulting reconstructions for both one and two ink coated hairs can be seen in Fig. 6.3. Because the hairs were too small to move about precisely in the propagation medium, the whole mirror and cell assembly was moved instead. The photodiodes could not be moved, because the beam expanders had been removed to increase the interrogation laser intensity. Moving the sensing mirror necessitated making a calibration for each new mirror position. To decrease acquisition time, calibrations were made every 10 positions instead, and the minimum and maximum output voltages were interpolated. This resulted in non exact scaling, which is apparent in the oscillation in the x direction of detected pressure in Fig. 6.3.

The reconstructions of both the images taken of hair show that the resolution is far too low

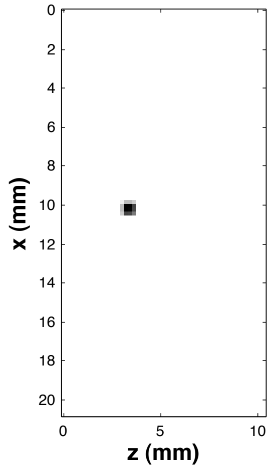

(a) Simulated initial absorption cross section.

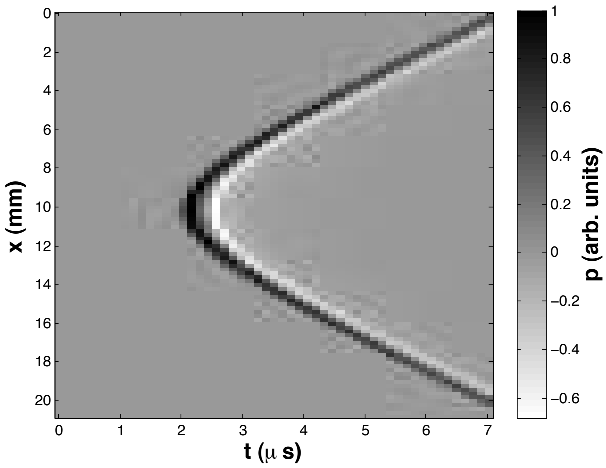

(b) Simulated detected pressure distribution.

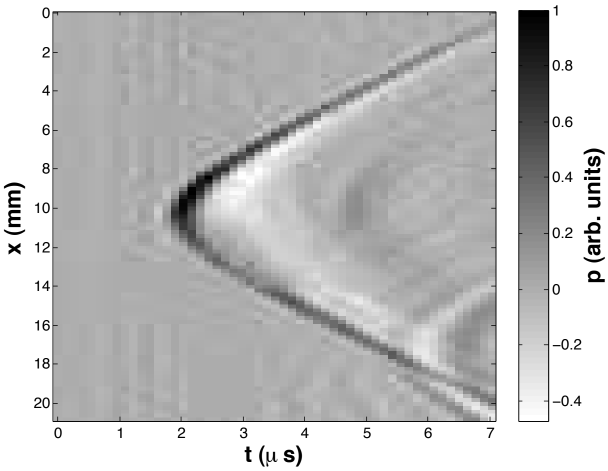

(c) Actual detected pressure distribution.

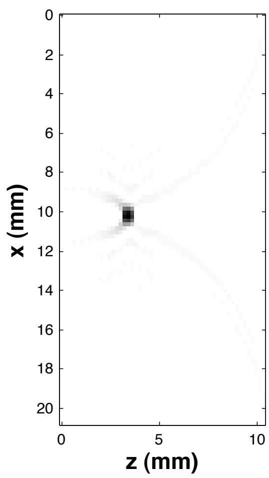

(d) Reconstruction using simulated data.

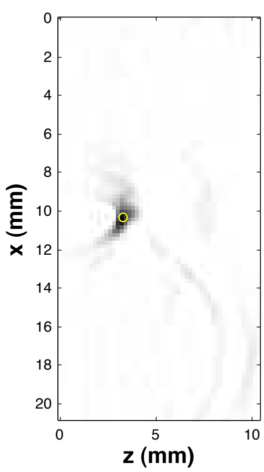

(e) Reconstruction using actual data.

Figure 6.1: A comparison between simulated and actual reconstructions for a simple phantom. The actual reconstruction is spread out more than the simulated one, though both have the same qualitative features. The actual absorber position and size is shown as a yellow circle in Fig.6.1e

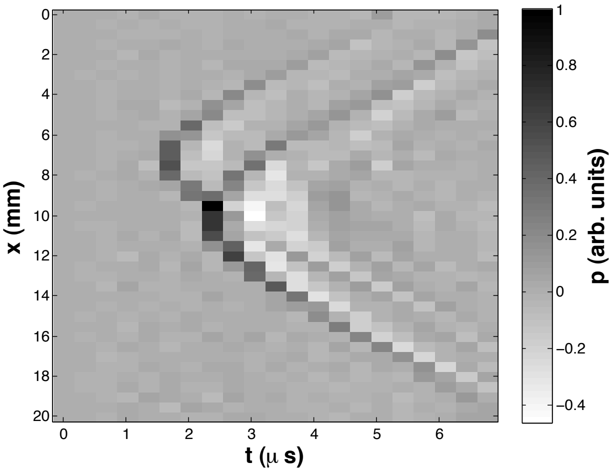

(a) Detected pressure for two absorbers.

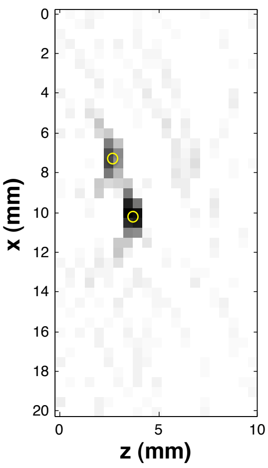

(b) Reconstructed image of two absorbers.

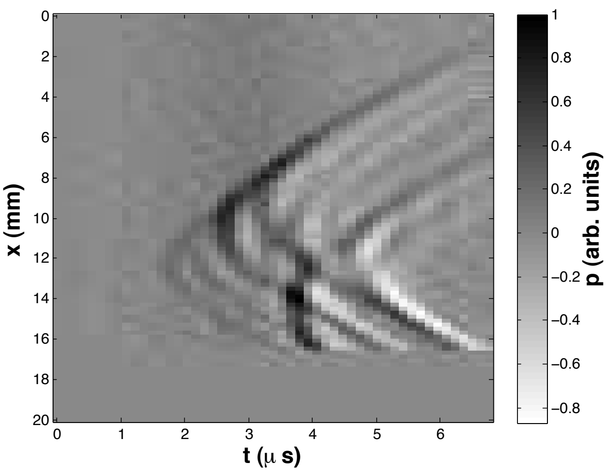

(c) Detected pressure for four absorbers.

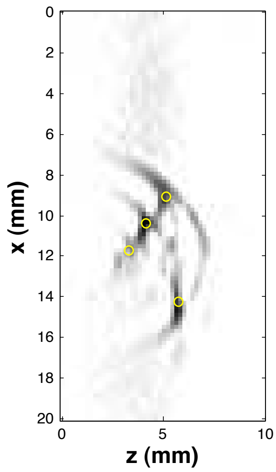

(d) Reconstructed image of four absorbers.

Figure 6.2: Reconstructions of more complex configurations of ink filled silicon tube absorbers.

to resolve the individual hair. In these scans, the aperture diameter was 200 μm, and the step size was 50 μm, so it is unsurprising that the 70 μm hairs could not be resolved. However, it was expected that the resolution would be better than the ≈ 500 μm achieved. This is possibly a result of the comparatively large anomalous signal due to the interactions between the sensing mirror and the excitation laser, which was discussed in Sec. 5.2. The oscillation in calculated pressure amplitude would also have a negative effect on resolution, though to what extent is unknown.

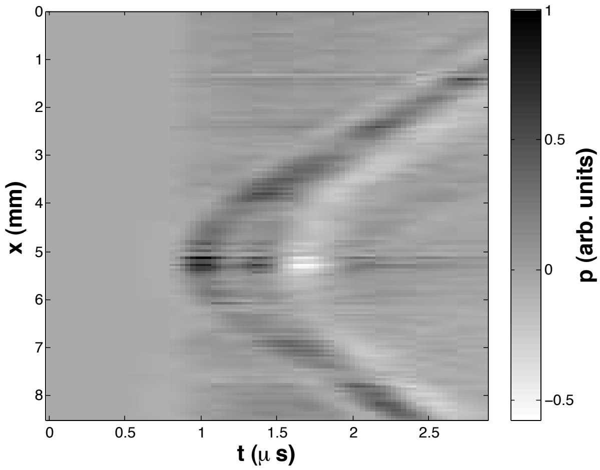

(a) Detected pressure for a single inked hair.

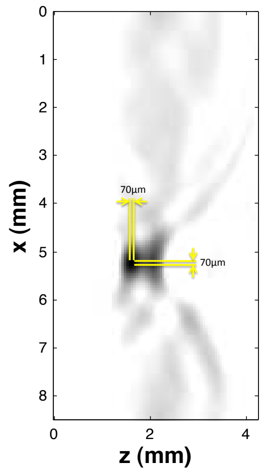

(b) Reconstructed image of a single inked hair.

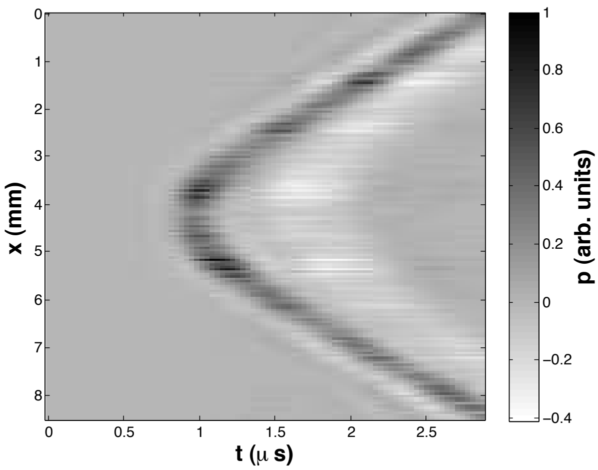

(c) Detected pressure for two inked hair.

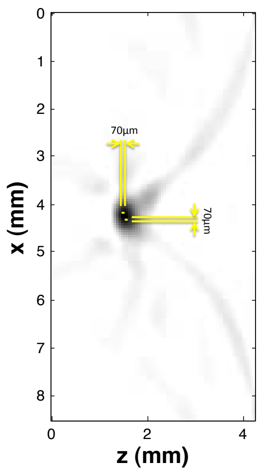

(d) Reconstructed image two single inked hair.

Figure 6.3: Reconstructions of single, and multiple ink covered hairs. The resolution is insufficient to properly resolve the individual hairs.

Chapter 7

Conclusions

This project set out to develop a new detector for the purposes of photoacoustic tomography. The detector design was based on a Michelson interferometer with quadrature phase detection, where one of the interferometer mirrors served as the ultrasound sensor. It was shown that all current PA detector technologies have limitations, either in terms of sensitivity, data acquisition speed, or resolution. The prototype system developed in this project was limited in all three of these areas, however it was discussed how future iterations could easily satisfy both the resolution, and acquisition speed criteria. The requirement of sensitivity is possibly more difficult to address, as this is a frequency dependent quantity. However, it was shown theoretically, that in frequency range studied in this project, the Michelson sensor is several times more sensitive than the only other detection system that satisfies both the resolution and acquisition speed requirements.

While the quadrature phase detection component of the system worked as expected, there were several difficulties with the sensing mirror which had to be overcome. Firstly, it was shown that the substrate of the mirror had to be thick enough so that acoustic waves entering the substrate would not reflect off internal boundaries and interfere with the oncoming signal. It was also shown that a very thin substrate avoided this problem, since it acted acoustically as a single plane.

It was then seen that thick, solid substrates were unsuitable for use as the sensor because oncoming PA waves generated Rayleigh waves on the surface, which interfered with any subsequent PA signal. Again, the very thin mirror avoided this problem, because it was not thick enough to support Rayleigh waves.

The final sensor assembly consisted of a 150 μm substrate, mirror coated on one side, and bonded around the perimeter to a rigid optical flat. This was found to be interferometrically stable, and could reliably detect PA signals, despite displaying some anomalous response to the excitation laser.

The simulated PA disturbances matched well with experiment, and were used to validate the implementation of the reconstruction algorithm. The algorithm successfully reconstructed experimental data, to produce 2D photoacoustic images of horizontally symmetric blood vessel phantoms.

The PA images created had resolutions of less than 1 mm to imaging depths of 6 mm, however it is expected that an increase in resolution should be relatively simple to achieve with refinements to the apparatus.

Future Work

This project was focused on implementing a novel type of detector for photoacoustic imaging. The focus was on proving that the suggested system could actually function as intended, rather than trying to optimise parameters such as resolution. In this respect, the project has been an unqualified success. A Michelson interferometer with quadrature phase detection, can act as a photoacoustic imaging system, given a suitably designed sensing mirror.

Future work will focus on optimising the components which were developed in this project, so the system can be implemented in real world situations.

The first step to this would be to produce a higher quality sensing mirror. The mirror substrate made from the 150 μm glass coverslip needs to be replaced with an optically flat, and preferably thinner substrate. This would automatically increase optical modulation by creating larger, more well defined interference fringes.

The gold mirror coating needs to be replaced with a dichroic coating, which transparent to the excitation wavelength. This should hopefully remove the only unresolved problem with the sensing mirror, which was the signal due to the excitation laser. This would also allow illumination and detection to occur at the same place, thus increasing signal strength.

The optical flat to which the mirror is bonded needs to be anti-reflection coated to remove the etalon cavity effect. This would remove a source of uncertainty in calculated mirror displacement.

The extension of the current system to produce 3D images is trivial, as it simply requires data to be taken over a plane, rather than a single line. Ideally, this would be achieved by replacing the photodiodes with nanosecond gated CCDs or fast framing cameras. Use of CCDs would also automatically reduce the effective step size and aperture size to that of an individual pixel, and so would drastically increase resolution.

The implementation of the reconstruction algorithm needs to be improved, and could also be extended to include effects of finite detector element size.

The HeNe interrogation could be replaced with a UV diode laser. This would approximately double the sensitivity of the detector due to the reduced wavelength.

The system needs to be tested on more realistic phantoms, and ultimately on living human tissue. This would allow the performance of this detection system to be directly compared with others. It would also give an indication as to the plausibility of this system being considered for use in routine medical imaging.

Finally, it would also be necessary to construct the interferometer on a rigid movable 'wand', rather than on an optics table. This would allow development of methods to stabilise the interferometer, which would be needed for real clinical imaging.

Acknowledgements

I would like to sincerely thank Dr. Alexis Bishop for supervising me in this project. The vision, guidance and facilities he provided, allowed me to experience a truly fantastic, and fascinating range of experimental physics. I would also like to thank Naomi Schofield, whose assistance, and taste in music made the lab experience all the more enjoyable. Additionally, I wish to express my gratitude to the many other members of the school of physics who donated their time, experience, and equipment, which contributed to the success of this project. Special thanks to my student colleagues for the many enlightening conversations, and who have made the last four years an absolute pleasure. Finally, I wish to thank the many inspirational lecturing and teaching staff within the school, who have equipped me for this project, and the physics which I am eagerly awaiting in the future.

Appendix A

Mirror Manufacture

As mentioned already, the design of the sensing mirror went through several changes during the course of the project, due to both expected, and unforeseen problems. The ability to manufacture the mirrors in a short time frame, on site, and at low cost, was therefore a key factor in the success of the project.

Mirror Polishing

One approach to creating a mirror which would not propagate Rayleigh waves was to choose a material which increased the rate at which energy in these waves would radiate back into the propagation medium, or 'leakiness'. The leakiness of a material depends on several properties, but as a general guide, the more acoustically similar the solid is to the adjoining liquid, the greater the leakiness. Polymers are desirable in this respect, due to their low densities, and relatively low elastic moduli.

Thick slabs of polymethyl methacrylate (PMMA) were available which already had a suitable surface finish. PMMA however has quite a high density and elastic moduli for a polymer, so it was desirable to test polycarbonate (PC) and cross linked polystyrene (CLPS) as well.

The PC and CLPS substrates were initially machined into 25 mm cylinders, of about 30 mm in length. A PMMA substrate was also prepared in this way for comparison. A polishing 'puck' was also created, which was a large metal disc with a hole through the centre for the substrates to slide into. The puck had a very flat bottom, and was designed to hold the substrate extremely flat during polishing. This was necessary because the surfaces had to be both shiny and interferometrically flat.

Substrates were first polished by hand on silicon carbide polishing paper. Once all striations from machining had been removed, a fabric pad with diamond paste was used on a rotating polisher. This was found to produce a better surface finish than polishing paper alone. It was extremely difficult to obtain a high quality finish with the any of the polymers used. A

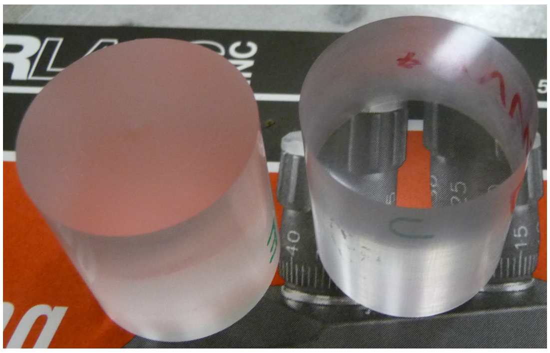

Figure A.1: The above shows two PMMA substrates. The rough finish on the left substrate was the result of machining. The surface finish on the right was achieved after polishing. Small scratches in the polished surface can still be seen, owing to the difficulty of polishing polymers.

comparison between a polished and unpolished PMMA substrate can be seen in Fig. A.1.

Mirror Coating

Mirror coatings were applied to the polished polymer substrates, and also to non-standard glass substrates. In both cases, the mirror surface was applied by sputter coating gold onto the surface. Ideally, the coatings would have been dichroic so as to be transparent to the excitation laser, however the gold coating offered a rapid, and cheap alternative, which was invaluable for prototyping. Also, the reflectance of gold is greater than 95% at the 633 nm wavelength light being used as the interrogation beam.

The coater itself was usually used for sample preparation in scanning electron microscopy, however it could deposit sufficiently thick layer of gold in around four minutes of continuous coating. Continuous coating was suitable for the glass substrate, as the thermal load resulted in a temperature rise which was far below the glass transition temperature. The situation was different for the polymer substrates which were coated. Continuous coating raised the temperature of the polymer substrates to a point where they distorted. This was clearly unacceptable, as the mirrors needed to be interferometrically flat. The solution was to coat the substrates for only 30 seconds at a time, with a 15 minute cooling down period between each coat. This ensured the temperature of the substrate never rose more than a few degrees, and so did not become warped. The difference between a heat affected and unaffected coated substrate can be seen in Fig. A.2.

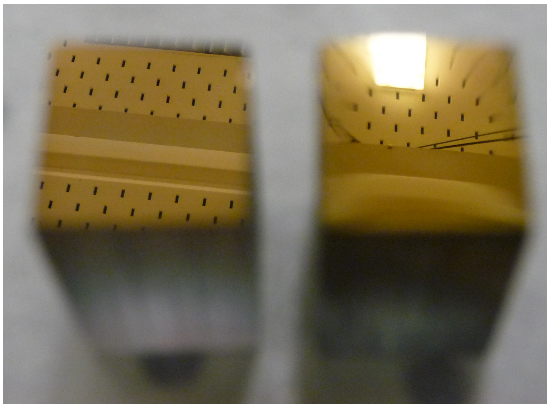

Figure A.2: The above shows two substrates of PMMA cut from a single block. The right substrate was coated continuously for 4 minutes. It shows substantial thermal deformation around its edge. The left substrate was coated in 30 second increments, with cooling time between. It shows no sign of distortion.

Bibliography

[1] G. Tearney, M. Brezinski, B. Bouma, S. Boppart, C. Pitris *et al.*, "In vivo endoscopic optical biopsy with optical coherence tomography", *Science*, **276**, no. 5321, pp. 2037–2039 (1997).

[2] D. Huang, E. Swanson, C. Lin, J. Schuman, W. Stinson *et al.*, "Optical coherence tomography", *Science*, **254**, no. 5035, pp. 1178–1181 (1991).

[3] S. N. Roper, M. D. Moores, G. V. Gelikonov, F. I. Feldchtein, N. M. Beach *et al.*, "In vivo detection of experimentally induced cortical dysgenesis in the adult rat neocortex using optical coherence tomography.", *Journal of neuroscience methods*, **80**, pp. 91–98 (1998).

[4] M. Xu and L. Wang, "Photoacoustic imaging in biomedicine", *Review of Scientific Instruments*, **77**, p. 041101 (2006).

[5] M. Xu, Y. Xu and L. V. Wang, "Time-domain reconstruction algorithms and numerical simulations for thermoacoustic tomography in various geometries.", *IEEE transactions on bio-medical engineering*, **50**, no. 9, pp. 1086–1099 (2003).

[6] A. Rosencwaig, "Photoacoustic spectroscopy of solids", *Optics Communications*, **7**, no. 4, pp. 305–308 (1973).

[7] L. Wang, "Prospects of photoacoustic tomography", *Medical physics*, **35**, no. 12, pp. 5758–5767 (2008).

[8] J. Laufer, E. Zhang and P. Beard, "Quantitative in vivo measurements of blood oxygen saturation using multiwavelength photoacoustic imaging", *Proc. SPIE*, **6437**, p. 64371Z (2007).

[9] B. Cox, J. Laufer and P. Beard, "The challenges for quantitative photoacoustic imaging", *Proc. SPIE*, **7177**, p. 717713 (2009).

[10] E. Zhang and P. Beard, "2D backward-mode photoacoustic imaging system for NIR (650-1200nm) spectroscopic biomedical applications", *Proc. SPIE*, **6086**, pp. 60860H1–8 (2006).

[11] G. Ku and L. Wang, “Deeply penetrating photoacoustic tomography in biological tissues enhanced with an optical contrast agent”, *Optics letters*, **30**, no. 5, pp. 507–509 (2005).

[12] A. Oraevsky, V. Andreev, A. Karabutov and R. Esenaliev, “Two-dimensional optoacoustic tomography: transducer array and image reconstruction algorithm”, *Proc. SPIE*, **3601**, pp. 256–267 (1999).

[13] T. Allen, B. Cox, P. Beard and L. Street, “Generating photoacoustic signals using high-peak power pulsed laser diodes”, *Proc. SPIE*, **5696**, pp. 233–242 (2005).

[14] K. Maslov and L. Wang, “Photoacoustic imaging of biological tissue with intensity-modulated continuous-wave laser”, *Journal of Biomedical Optics*, **13**, no. 2, p. 024006 (2008).

[15] A. K. V.E. Gusev, *Laser Optoacoustics*, New York: American Insitiute of Physics (1993).

[16] F. A. Duck, *Physical Properties of Tissue*, London: Academic Press (1990).

[17] L. Song, K. Maslov, R. Bitton, K. Shung and L. Wang, “Fast 3-D dark-field reflection-mode photoacoustic microscopy in vivo with a 30-MHz ultrasound linear array”, *Journal of biomedical optics*, **13**, no. 5, p. 054028 (2008).

[18] A. A. Oraevsky and A. A. Karabutov, *Biomedical photonics handbook*, Boca Raton: CRC Press, chap. 34 (2003).

[19] G. Paltauf and P. E. Dyer, “Photomechanical processes and effects in ablation.”, *Chemical reviews*, **103**, no. 2, pp. 487–518 (2003).

[20] J. Blitz, *Fundamentals Of Ultrasonics*, Butterworths Co., London (1963).

[21] “Temporal backward projection of optoacoustic pressure transients using Fourier transform methods”, *Phys. Med. Biol.*, **46**, pp. 1863–1872 (2001).

[22] P. Burgholzer, G. Matt, M. Haltmeier and G. Paltauf, “Exact and approximative imaging methods for photoacoustic tomography using an arbitrary detection surface”, *Phys. Rev. E*, **75**, no. 4, p. 046706 (2007).

[23] M. Agranovsky and P. Kuchment, “Uniqueness of reconstruction and an inversion procedure for thermoacoustic and photoacoustic tomography with variable sound speed”, *Inverse Problems*, **23**, no. 5, pp. 2089–2102 (2007).

[24] P. Kuchment and L. Kunyansky, “Mathematics of thermoacoustic tomography”, *European Journal of Applied Mathematics*, **19**, no. 02, pp. 191–224 (2008).

[25] H. Zhang, K. Maslov, M. Li, G. Stoica and L. Wang, "In vivo volumetric imaging of subcutaneous microvasculature by photoacoustic microscopy", *Opt. Express*, **14**, no. 20, pp. 9317–9323 (2006).

[26] V. Tuchin, *Tissue Optics*, SPIE Press, Washington, 2nd edn. (2007).

[27] E. Zhang, J. Laufer and P. Beard, "Backward-mode multiwavelength photoacoustic scanner using a planar Fabry-Perot polymer film ultrasound sensor for high-resolution three-dimensional imaging of biological tissues", *Applied Optics*, **47**, no. 4, pp. 561–577 (2008).

[28] P. Beard, E. Zhang and B. Cox, "Transparent Fabry-Perot polymer film ultrasound array for backward-mode photoacoustic imaging", *Proc. SPIE*, **5320**, pp. 230–237 (2004).

[29] G. M. Hale and M. R. Querry, "Optical Constants of Water in the 200-nm to 200-microm Wavelength Region.", *Applied Optics*, **12**, no. 3, pp. 555–563 (1973).

[30] M. Firbank, M. Hiraoka, M. Essenpreis and D. T. Delpy, "Measurement of the optical properties of the skull in the wavelength range 650-950 nm.", *Phys. Med. Biol.*, **38**, no. 4, pp. 503–510 (1993).

[31] P. Beard, "Photoacoustic imaging of blood vessel equivalent phantoms", *Proc. SPIE*, **4618**, pp. 54–62 (2002).

[32] S. Mallidi, A. Karpiouk, S. Aglyamov, S. Sethuraman and S. Emelianov, "Measurement of blood perfusion using photoacoustic, ultrasound and strain imaging", *Proc. SPIE*, **6437**, p. 643707 (2007).

[33] C. Hoelen, F. De Mul, R. Pongers and A. Dekker, "Three-dimensional photoacoustic imaging of blood vessels in tissue", *Optics letters*, **23**, no. 8, pp. 648–650 (1998).

[34] E. Zhang, J. Laufer and P. Beard, "Three dimensional photoacoustic imaging of vascular anatomy in small animals using an optical detection system", *Proc. SPIE*, **6437**, p. 64370S (2007).

[35] H. Fang and L. Wang, "Photoacoustic Doppler flowmetry", *Proc. SPIE*, **6856**, p. 68561M (2008).

[36] Standards New Zealand, *Safety of laser products Part 4: Laser guards*, snz as/nzs 2211.4 edn. (2002).

[37] A. B. Bhatia, *Ultrasonic Absorption*, Oxford University Press, London (1967).

[38] P. N. T. Wells, *Biomedical Ultrasound*, Academic Press, London (1977).

[39] W. P. Mason, *Physical Acoustics and the Properties of Solids*, D. Van Nostrand Company, Inc., New Jersey (1958).

[40] Y. Nakamura, "Absorption Measurements of Ultrasonic waves in plastic sheets", *Journal of Applied Physics*, **34**, no. 11, pp. 3288–3290 (1963).

[41] V. A. Shutilov, *Fundamental Physics of Ultrasound*, Gordon and Breach Science Publishers, New York (1988).

[42] S. Huang, Y. Hou, S. Ashkenazi and M. ODonnell, "High-resolution ultrasonic imaging using an etalon detector array", *Applied Physics Letters*, **93**, no. 11, p. 113501 (2008).

[43] E. Z. Zhang, P. C. Beard, J. G. Laufer and R. B. Pedley, "In vivo high-resolution 3D photoacoustic imaging of superficial vascular anatomy", *Physics in medicine and biology*, **54**, no. 4, pp. 1035–1046 (2009).

[44] A. Oraevsky, S. Jacques and F. Tittel, "Measurement of tissue optical properties by time-resolved detection of laser-induced transient stress", *Applied Optics*, **36**, no. 1, pp. 402–415 (1997).

[45] C. Hoelen and F. de Mul, "Image reconstruction for photoacoustic scanning of tissue structures", *Applied Optics*, **39**, no. 31, pp. 5872–5883 (2000).

[46] J. Niederhauser, M. Jaeger, M. Hejazi, H. Keppner and M. Frenz, "Transparent ITO coated PVDF transducer for optoacoustic depth profiling", *Optics Communications*, **253**, no. 4-6, pp. 401–406 (2005).

[47] E. Hecht, *Optics*, Addison Wesley, 4th edn. (2002).

[48] G. Paltauf and H. Schmidt-Kloiber, "Measurement of laser-induced acoustic waves with a calibrated optical transducer", *Journal of Applied Physics*, **82**, no. 4, p. 1525 (1997).

[49] G. Paltauf, H. Schmidt-Kloiber, K. P. Kostli and M. Frenz, "Optical method for two-dimensional ultrasonic detection", *Applied Physics Letters*, **75**, no. 8, p. 1048 (1999).

[50] A. Ben-Yakar and R. Hanson, "Ultra-fast-framing schlieren system for studies of the time evolution of jets in supersonic crossflows", *Experiments in Fluids*, **32**, no. 6, pp. 652–666 (2002).

[51] C. T. Chin, C. Lancee, J. Borsboom, F. Mastik, M. E. Frijlink *et al.*, "Brandaris 128: A digital 25 million frames per second camera with 128 highly sensitive frames", *Review of Scientific Instruments*, **74**, no. 12, pp. 5026–5034 (2003).

[52] I. A. Viktorov, *Rayleigh and Lamb Waves*, Plenum Press, New York (1967).

[53] S. Biwa, "Elastic properties of rubber particles in toughened PMMA: ultrasonic and micromechanical evaluation", *Mechanics of Materials*, **33**, no. 12, pp. 717–728 (2001).